



Structural, vibrational and thermodynamic properties of Mg_2SiO_4 and MgSiO_3 minerals from first-principles simulations



E.R. Hernández^{a,*}, J. Brodholt^b, D. Alfè^b

^a Instituto de Ciencia de Materiales de Madrid (ICMM-CSIC), Campus de Cantoblanco, 28049 Madrid, Spain

^b Department of Earth Sciences, University College London, Gower Street, London WC1E 6BT, Great Britain, United Kingdom

ARTICLE INFO

Article history:

Received 2 July 2014

Received in revised form 2 October 2014

Accepted 15 October 2014

Available online 6 November 2014

Keywords:

Mantle minerals

Thermodynamics of minerals

Mantle transition zone

First principles simulation

ABSTRACT

In this paper we report a computational study of the structural and vibrational properties of the Mg-end members *forsterite*, *wadsleyite* and *ringwoodite* of Mg_2SiO_4 , and *akimotoite*, *majorite* and the perovskite phase of MgSiO_3 . Our calculations have been carried out in the framework of Density Functional Theory (DFT) using a plane wave basis set and the Projector-augmented Wave (PAW) method to account for the core electrons. All structures have been fully relaxed at a series of volumes corresponding to the pressure range relevant to the transition zone in the Earth's mantle, and at each volume the phonon frequencies have been obtained and classified. Using the quasi-harmonic approximation, we have estimated a series of thermodynamic properties for each structure, including the Gibbs free energy, from which we have computed approximate phase diagrams for Mg_2SiO_4 and MgSiO_3 . In spite of our reliance on the quasi-harmonic approximation, which is expected to break down at high temperatures, our calculated phase diagrams qualitatively reproduce the main features expected from diagrams fitted to experimental data. For example, from the computed phase diagram for Mg_2SiO_4 we obtain a post-spinel boundary at $P = 22.1$ GPa at $T = 1873$ K, with a slope of -3.4 MPa/K. This supports experimental results suggesting a relatively large slope rather than those favouring a much flatter one. It also suggests that vertical deflections of the 660 km discontinuity due to thermal signatures from plumes and slabs should be similar to those at the 410 km, and that a deflection of 35 km as seen in recent seismic studies could be caused by a thermal anomaly as small as 330 K. We also identify the triple point between the ringwoodite, ilmenite (plus periclase) and perovskite (plus periclase) phases to be at $P = 22.9$ GPa and $T = 1565$ K. Our results clearly illustrate the stringent requirements made on theoretical models in order to extract predictions compatible with the available experimental data.

© 2014 Elsevier B.V. All rights reserved.

1. Introduction

Our understanding of the internal structure and dynamics of the Earth and similar planets builds up through the constructive interplay of geophysical observation (mostly of seismography data) and mineral physics. Geophysical observation has resulted in a wealth of data on the variation of S and P waves and the density as a function of depth, but does not provide direct information on composition or temperature. It has long been recognised, however, that the layered internal structure of the Earth, as revealed by seismological data analysis, correlates with the occurrence of a series of phase transitions in its material constituents. Indeed, the upper-mantle ("410 km") discontinuities are attributed to the olivine to β -spinel

(wadsleyite) and γ -spinel (ringwoodite) phase transitions; likewise, the transition zone-to-lower mantle discontinuity is thought to arise from the post-spinel disproportionation reaction, in which the ringwoodite γ -spinel structure of $(\text{Mg}_{1-x}, \text{Fe}_x)_2\text{SiO}_4$ decomposes into $(\text{Mg}_{1-y}, \text{Fe}_y)\text{SiO}_3$ plus ferropericlase (Bina and Helffrich, 1994). In this respect, one of the aims of mineral physics is to propose compositional models that can reproduce/explain the geophysical observations, thus gaining a more detailed understanding of the nature of the observed seismic transitions and of how these correlate with chemical composition in the mantle. However, the experimental task required for this is a daunting one, given the range of possible compositions, the technical difficulties involved in reproducing the temperature and pressure conditions that are relevant to the Earth's interior, and in carrying out controlled experiments at such conditions. Nevertheless, given the geophysical relevance of these materials, it is not surprising that a great number of experimental as well as theoretical studies have

* Corresponding author.

E-mail addresses: Eduardo.Hernandez@csic.es (E.R. Hernández), J.Brodholt@ucl.ac.uk (J. Brodholt), D.Alfe@ucl.ac.uk (D. Alfè).

been devoted to the understanding of their thermodynamics in general, and their phase dynamics in particular (see e.g. [Stixrude and Lithgow-Bertelloni, 2011](#), [Wentzcovitch et al., 2010](#) and references therein).

In this article we report the results of an extensive computational study based on Density Functional Theory (DFT) ([Hohenberg and Kohn, 1964](#); [Kohn and Sham, 1965](#)) of the structural and dynamic properties of various phases of composition Mg_2SiO_4 and MgSiO_3 relevant to the transition zone of the Earth's mantle. We have determined the Gibbs free energy of each phase on the basis of the quasi-harmonic approximation, and used those free energies to obtain qualitative phase diagrams for these systems.

There are a number of reasons that make this a worthwhile approach. First of all, the entire phase diagram is predicted within exactly the same level of theory, and by comparing with experimental data, provides a stringent test of these methods. Secondly, we shown how small uncertainties in free energies affect the phase boundaries and slopes, again providing valuable insight into how sensitive phase boundaries are to DFT uncertainties. And thirdly, there are aspects of the phase diagram which are still uncertain. These include the position of triple points, but also the Clapeyron slope of the ringwoodite to perovskite plus periclase phase transition. This is geophysically important in that the magnitude of the slope affects mantle flow between the upper and lower mantle. Moreover, the magnitude of the slope has implications for seismic detection of the deflection of the phase boundaries due to thermal signatures of plumes and slabs.

The structure of this paper is the following: in Section 2 we describe the computational approach used in this study. Section 3 is devoted to a detailed discussion of our results; first, in Section 3.1 we describe the structures obtained through relaxation calculations for each phase; secondly, Section 3.2 is devoted to a discussion of the vibrational properties. In the interest of space we only discuss in detail the cases of forsterite (Mg_2SiO_4) and the orthorhombic perovskite phase of MgSiO_3 , as representative cases of each composition. The vibrational properties of the remaining phases are discussed in an appendix at the end of this paper, except in the cases of majorite, MgO (periclase) and SiO_2 (stishovite), which are reported in a [supplementary information file](#). Our calculated phase diagrams are reported in Section 3.3, where we compare them to the available experimental and previous theoretical data. Finally, in Section 4 we summarise our results and conclusions.

2. Computational methodology

Our calculations have been carried out using the VASP code ([Kresse and Furthmüller, 1996](#)), an efficient program for performing DFT simulations using a plane-wave basis set, combined with the Projector augmented Wave (PAW) method ([Blöchl, 1994](#)), which enables VASP to perform all-electron calculations ([Kresse and Joubert, 1999](#)) within this framework. The code uses an efficient charge-density extrapolation technique ([Alfè, 1999](#)) which enables it to reduce the number of self-consistency cycles required in subsequent steps of a molecular dynamics or structural relaxation simulation.

Our calculations have been performed employing the Perdew-Wang (PW91) Generalized Gradient Approximation (GGA) functional ([Wang and Perdew, 1991](#)) to account for the exchange-correlation energy. While it is well-known that the use of the Local Density Approximation (LDA) to the exchange-correlation energy generally results in equilibrium lattice parameters and volumes that match more closely their experimental counterparts than those predicted by GGA functionals, it is also well-established that the position of LDA-calculated phase boundaries is much worse,

Table 1

The structures considered in this study. Listed is the chemical composition of each structure, the number of formula units per primitive unit cell, the Monkhorst-Pack sampling used in each case, and the number of k-points in which it resulted.

Structure	Composition	f.u./u.c.	k-point grid	Nr. k-points
Forsterite (fo)	Mg_2SiO_4	4	$6 \times 4 \times 6$	18
Wadsleyite (wa)	Mg_2SiO_4	4	$4 \times 4 \times 4$	17
Ringwoodite (ri)	Mg_2SiO_4	2	$8 \times 8 \times 8$	60
Akimotoite (ak)	MgSiO_3	2	$8 \times 8 \times 8$	88
Majorite (mj)	MgSiO_3	16	$4 \times 4 \times 4$	14
Perovskite (pv)	MgSiO_3	4	$6 \times 6 \times 4$	18
Periclase (pe)	MgO	1	$8 \times 8 \times 8$	60
Stishovite (st)	SiO_2	2	$8 \times 8 \times 10$	50

sometimes being underestimated by ~ 10 GPa or more (see e.g. [Yu et al., 2007, 2008, 2011](#)). Since our primary aim in this study is to determine the phase diagrams of Mg_2SiO_4 and MgSiO_3 , we have resorted to using a GGA functional. A kinetic energy plane-wave cutoff of 500 eV has been used in our simulations; it will be shown below that this is sufficient to converge energy and enthalpy differences between the various structures considered in this study, and is also sufficient for adequately converging the atomic forces, a requirement for the phonon calculations to be discussed below. Since all the minerals we have concerned ourselves with in this study have sizeable band gaps at the Fermi energy,¹ requirements on the k-point sampling have not been large. In [Table 1](#) the actual k-point sampling grids ([Monkhorst and Pack, 1976](#)) used for each structure are listed. Also listed in the table is the number of formula units per primitive cell for each structure. We note that for computational convenience and expedience the calculations reported below have all been performed on primitive cells of the corresponding structures, even in the cases such as ringwoodite, wadsleyite, akimotoite and majorite, for which experimental structures are usually quoted in a conventional unit cell, several times larger than the primitive one.

With the above set-up, our strategy has been to conduct an initial series of fixed-volume structural relaxations for each system at different volumes. In some cases, such as ringwoodite (a cubic structure) the relaxation involved only internal (atomic) coordinate variables, but in general lattice parameters have also been relaxed in order to attain a hydrostatic pressure at each volume. From these initial calculations we were able to obtain for each structure a sequence of volumes corresponding to pressures in the range ≈ -20 to 30 GPa at intervals of ~ 2.5 GPa. It was necessary to consider volumes corresponding to negative pressures so as to appropriately account for the thermal expansion at finite temperatures (see below). Each of these configurations were then carefully relaxed at each volume, with a view to perform a phonon calculation using the small displacements method implemented in the PHON code ([Alfè, 2009](#)). Each structure was relaxed until forces on all atoms were smaller than 10^{-6} eV/Å, in order to ensure that the calculated phonon frequencies were unaffected by numerical noise in the forces. These calculations provided us with phonon band structures and vibrational densities of states (VDOS), as well as with a quasi-harmonic approximation to the vibrational free energy for each structure and each volume considered, from which we were then able to construct an approximate phase diagrams for the Mg_2SiO_4 and MgSiO_3 systems, which constitute the central result of this work.

¹ The gap in forsterite at 0 GPa is calculated to be ~ 5 eV, and actually increases slightly within the pressure range considered here; the same occurs for wadsleyite and ringwoodite, which have comparable gap sizes; MgSiO_3 in the perovskite structure has a larger gap, ~ 5.8 eV at 0 GPa, which also shows a tendency to increase with pressure; akimotoite has a similar sized gap, while that of majorite is comparable to the gaps of the Mg_2SiO_4 structures).

3. Results

3.1. Structural relaxation

Fig. 1 shows the variation of the total energy as a function of volume for the Mg_2SiO_4 and MgSiO_3 structures considered in this work. Two sets of data are shown for each structure; the dashed lines represent results obtained with a plane wave cutoff of 500 eV, while the continuous lines in the same colour show data obtained for the same structure, but with a cutoff of 1000 eV, similar to that used by Yu et al. (2008) for their determination of the phase boundaries between forsterite, wadsleyite and ringwoodite. It is obvious from the data shown in Fig. 1 that the total energy is not fully converged with the lower plane wave cutoff, though the differences in total energy are small (in all cases smaller than 0.04 eV/f.u.). It should be stressed, however, that our results do not rely on the full convergence of the total energy, but on that of the energy differences between the various structures. That energy differences are fully converged for this system with a plane wave cutoff of 500 eV is argued below and demonstrated in Fig. 2. By fitting the data plotted in Fig. 1 to the Murnaghan (Murnaghan, 1944) or Birch-Murnaghan (Birch, 1947) equation of state we can obtain values for the equilibrium volume, bulk modulus and its pressure derivative for each of the structures in this study. A selection of the data obtained is reported in Table 2. The differences in equilibrium volume and bulk modulus obtained when using either equation of state are small and fairly systematic (the equilibrium volume increases by an amount of the order of 0.01%, while the bulk modulus reduces by an amount smaller than 1%), so we only quote the data obtained by fitting to the Birch-Murnaghan equation of state. The effect of increasing the plane wave cutoff from 500 to 1000 eV is generally to reduce the equilibrium volume by an amount smaller than 0.1% (except in the case of the perovskite structure, which increases its volume by 0.03%), and to change the bulk modulus by about 1% (again with the exception of perovskite, which increases it by $\sim 2.5\%$).

Together with our calculated results, Table 2 lists a selection of data from previous theoretical as well as experimental studies for comparison. Most of the previous computational studies have been performed with the local-density approximation (LDA) to the exchange-correlation energy, although we also quote data from a study (Ottonello et al., 2009) that used the B3LYP (Becke, 1993; Stephens et al., 1994) hybrid functional, and from another one (Yu et al., 2011) using the generalised-gradient functional due to Perdew et al. (1996) (PBE). Overall, it can be seen from Table 2 that there is reasonable agreement, within well-known trends, of our

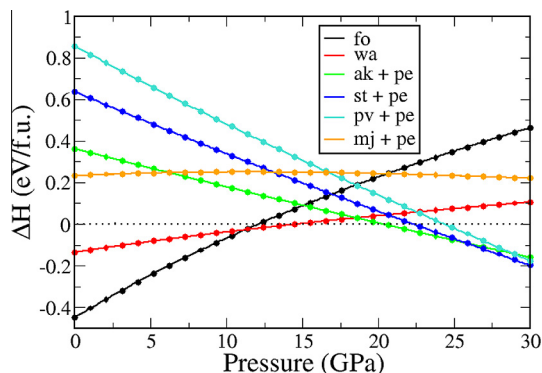


Fig. 2. Enthalpy vs pressure for all structures considered in this study. The enthalpies are referred to that of ringwoodite. Two sets of data are shown for each case: a continuous line, evaluated with a plane wave cutoff of 500 eV, and thick dots of the same colour, evaluated at 1000 eV cutoff. The enthalpy of periclase (pe) has been added to that of the structures with MgSiO_3 composition (twice to that of stishovite, SiO_2) to account for the difference in chemical composition with the Mg_2SiO_4 structures. Keys: ak = akimotoite; fo = forsterite; mj = majorite; pe = periclase; pv = perovskite; st = stishovite; wa = wadsleyite.

data with the results of previous simulation studies. LDA data for equilibrium volumes slightly under-estimates the experimental volumes. Our own volume values are larger than the LDA calculated data typically by 1–3%. Agreement is closer with the B3LYP results of Ottonello et al. (2009) for the Mg_2SiO_4 structures, which our own results overshoot by less than 1%. Conversely, bulk moduli obtained with either the LDA or B3LYP functionals are generally slightly higher than ours, while its pressure derivative seems to be rather insensitive to the calculation model, having a value that oscillates around 4. Concerning the comparison with available experimental data, we observe that our calculated equilibrium volumes tend to over-estimate the experimental values by about 2.5–3%, which is in line with the well-known over-estimation of lattice parameters by $\sim 1\%$ of the PW91 GGA functional used in our calculations. The trend is less clear on the bulk moduli prediction: although there seems to be a general tendency to under-estimate it by about 10%, in the case of ringwoodite the calculated value is larger by the same amount. Below we provide more detailed structural comparisons between the calculated structures and their experimental counterparts.

Let us now consider the question of the convergence of the total energy differences with respect to the employed plane wave cutoff. The relevant data is displayed in Fig. 2, where we have plotted enthalpies vs pressure rather than energies vs volume, so as to

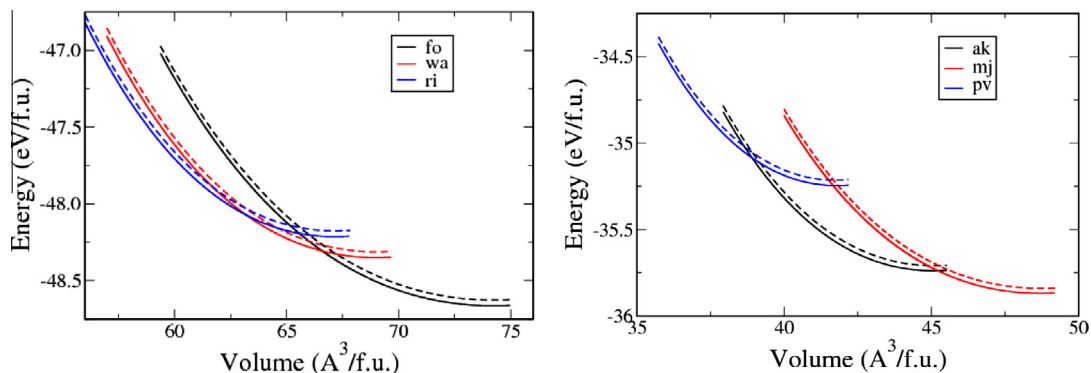


Fig. 1. Total energy vs volume. The left panel shows results obtained for structures with Mg_2SiO_4 composition, namely forsterite (fo), wadsleyite (wa) and ringwoodite (ri), while the right panel shows results for structures of MgSiO_3 composition, akimotoite (ak), majorite (mj) and the perovskite (pv) structure. Data shown with dashed and continuous lines of the same colour have been obtained for the same structure, but using a plane wave cutoff of 500 and 1000 eV, respectively. (For interpretation of the references to colour in this figure legend, the reader is referred to the web version of this article.)

Table 2
Equilibrium volumes of the unit cell (V_0), bulk modulus (B) and its pressure derivative for each structure, as obtained by fitting the calculated total energies of each structure [see Fig. 1] to the Birch–Murnaghan equation of state. The displayed calculated data has been obtained with a plane-wave cutoff of 1000 eV; data evaluated with a cutoff of 500 eV is very similar (see text) and is not shown. The experimental data is from the following references: a Hazen (1976); b Hazen et al. (2000); c Hazen et al. (1993); d Ye et al. (2012); e Yamanaka et al. (2005); f Angel et al. (1989); g Sinogeikin and Bass (2002); h Ross and Hazen (1990); i Jacobsen et al. (2008); j Yamanaka et al. (2002). Selected calculated values reported by other authors are from k Ottonello et al. (2009), obtained using the B3LYP functional, l Li et al. (2007) (LDA); m Wu and Wentzcovitch (2007) (LDA); n Yu and Wentzcovitch (2006) (LDA); o Karki (2002) (LDA); p Karki et al. (2000) (LDA); q Yu et al. (2011) (LDA); r Yu et al. (2011) (PBE); s Karki et al. (2000b) (LDA); t Oganov et al. (2005) (LDA).

Structure	Calculated			Experiment		
	V_0 (Å ³)	B (GPa)	dB/dP	V_0 (Å ³)	B (GPa)	dB/dP
Forsterite	297.4	117.4	4.42	288.6 ^a	120.0 ^a	–
	296.7 ^k , 289.5 ^l	130.8 ^k , 126.4 ^l	4.0 ^k , 4.2 ^l			
Wadsleyite	552.2	155.0	4.65	539.26 ^b	172.0 ^b	6.3 ^b
	550.4 ^k , 541.35 ^m	161.8 ^k , 165.7 ^m	4.4 ^k , 4.4 ^m			
Ringwoodite	537.5	175.2	4.28	525.73 ^c	159.0 ^d	6.3 ^d
	530.9 ^k , 527.5 ⁿ	196.4 ^k , 184.6 ⁿ	4.3 ^k , 4.5 ⁿ			
Akimotoite	270.65	188.4	4.6	262.6 ^e	219 ^e	4 ^e
	261.7 ^o , 271.8 ^f	210 ^o , 207.5 ^f	4.6 ^o , 3.7 ^f			
Majorite	1559.4	146.8	4.6	1518.6 ^g	166 ^g	4.2 ^g
	1519.2 ^h , 1584.4 ^f	160.8 ^g , 137.8 ^f	4.3 ^{g,f}			
Perovskite	167.2	229.7	4.4	162.36 ^h	254 ^h	4 ^h
	164.1 ^p , 169.7 ^f	247 ^p , 223.7 ^f	3.9 ^{p,f}			
Periclase	76.2	153.3	4.14	74.698 ⁱ	164 ⁱ	4.05 ⁱ
	75.24 ^s	159 ^s	4.30 ^s			
Stishovite	48.24	260.3	5.7	46.61 ^j	292 ^j	6 ^j
	46.31 ^t	318.33 ^t	4.37 ^t			

be able to show on the same graph the data for structures of Mg_2SiO_4 composition together with those of $MgSiO_3$ composition, by adding the enthalpy of MgO periclase to the latter. Again, two sets of data are shown for each structure: a continuous line showing data obtained with the lower cutoff, and dots of the same colour obtained with the larger cutoff. The enthalpies are referred to that of the ringwoodite structure.

The first observation to be extracted from Fig. 2 is that enthalpy (and hence total energy) differences are fully converged with a plane wave cutoff of 500 eV. Indeed it can be appreciated that the data obtained with both the lower and higher cutoffs fall neatly on top of each other in all the pressure range considered in this study. We can also see in Fig. 2 the sequence of phases predicted by our calculations in the low temperature limit of the phase diagram: in the pressure range 0–11.4 GPa forsterite is predicted to be the most stable structure, followed by wadsleyite from 11.4–14.5 GPa, then ringwoodite in the range 14.5 to 20.2 GPa, at which point akimotoite (plus periclase) becomes stable, followed by stishovite (plus periclase, $SiO_2 + 2MgO$) from 25.3 GPa onwards. Although not shown in the figure, which only goes up to 30 GPa, it is evident from the slopes of the enthalpy differences that at higher pressures ultimately the perovskite and periclase combination will become the most stable one. We should also note that the enthalpies displayed do not contain the zero-point vibrational contribution; although this contribution is not generally important at the temperatures relevant to the mantle, it can have a noticeable effect at low temperatures. In particular, the combination of stishovite plus periclase is practically wiped out of the phase diagram when this contribution is properly included [see Fig. 11]. A final observation to be derived from Fig. 2 is the fact that the majorite phase is never seen to be the most stable one at low temperature. This is consistent with the expectation that this phase is only stabilized at finite temperatures.

The low-temperature phase diagram of the Mg_2SiO_4 system is not known in detail, as experiments are usually conducted at higher temperatures. Nevertheless, inferences can be made from the high-temperature experimental data, and our zero-temperature results are not inconsistent with those. Comparing with

previous theoretical studies, Yu et al. (2008) have reported a fo-wa transition pressure of 6.5 GPa calculated with the LDA functional, and 12.6 GPa with the PBE–GGA functional; this latter figure is rather close to our estimation of 11.4 GPa. For the wa–ri transition they report values of 9.6 (LDA) and 15.7 GPa (PBE–GGA), the latter value again being close to our own result for this transition. To our knowledge, pressures for the ri–(ak+pe) and ak–(st+pe) transitions have not been hitherto evaluated.

Forsterite crystallizes in the orthorhombic crystal system, having space group $Pnma$ (Hazen, 1976). The structural parameters resulting from our relaxation calculation at 0 GPa are compared to an experimental structural determination reported by Hazen (1976) in Table 3. As already mentioned above, the theoretical lattice parameters over-estimate the experimental ones by a maximum of 1%, which is commonly the case with GGA functionals. This mismatch in the lattice parameters amounts to a 3% overestimation of the equilibrium volume. Otherwise, the atomic positions are satisfactorily reproduced, as seen in the table. The degree of agreement that is seen for the atomic positions in the case of forsterite is typical of what we find for the remaining structures considered in this study.

Table 3
Forsterite structural parameters, as obtained from our structural relaxation calculations at zero pressure, compared to the experimental structure obtained by Hazen (1976) at 77 K and 1 atm. For comparison with the experiment, data is listed here in the $Pbnm$ non-standard setting of space group $Pnma$.

Atom	Site	This work			Hazen (1976)		
		a (Å)	b (Å)	c (Å)	a (Å)	b (Å)	c (Å)
		4.793	10.283	6.020	4.746	10.18	5.976
		x	y	z	x	y	z
Mg	4a	0.0000	0.0000	0.0000	0.0000	0.0000	0.0000
Mg	4c	0.9917	0.2772	0.2500	0.9914	0.2772	0.2500
Si	4c	0.4265	0.0936	0.2500	0.4261	0.0939	0.2500
O	4c	0.7669	0.0916	0.2500	0.7661	0.0919	0.2500
O	4c	0.2224	0.4465	0.2500	0.2202	0.4469	0.2500
O	8d	0.2768	0.1629	0.0323	0.2777	0.1628	0.0333

The agreement observed between experimental and theoretically obtained lattice parameters is not confined to zero pressure. As an illustration of this, we show in Fig. 3 a comparison between the experimental data of Kudoh and Takeuchi (1985) and our calculated lattice parameters and volume up to pressures of 15 GPa. It is apparent that the over-estimation of the lattice parameters observed at zero pressure persists at higher pressures, but the response of the system to increasing pressures is nicely reproduced by the calculations. This is shown more quantitatively by comparing the experimental and calculated axial compressibilities, obtained by fitting the data shown in Fig. 3 to a first-order polynomial of the form $a(P) = (1 - \beta_a P)a(0)$ for lattice parameter a , and equivalently for b and c . Doing this with the experimental data results in $\beta_a = 1.36$, $\beta_b = 2.61$ and $\beta_c = 2.56 \times 10^{-3} \text{ GPa}^{-1}$, respectively, while from the theoretical data we obtain values of $\beta_a = 1.56$, $\beta_b = 2.61$ and $\beta_c = 2.13 \times 10^{-3} \text{ GPa}^{-1}$. It is interesting to note that the axial compressibilities along b and c , i.e. along the larger lattice parameters, are significantly larger than along a . The same procedure applied to the volume leads to a compressibility value of $\beta_v = 6.4 \times 10^{-3} \text{ GPa}^{-1}$ for the experimental data, compared to $\beta_v = 6.1 \times 10^{-3} \text{ GPa}^{-1}$ for the calculated volumes.

Also displayed in Fig. 3 (right panel) is the volume-vs.-pressure curve (shown in green) obtained by fitting the calculated data obtained by Li et al. (2007) (calculated at 300 K using the LDA approximation) to a third-order Birch-Murnaghan equation of state (Birch, 1947). This curve is very similar to the one we obtain, but shifted downward, giving a closer match to the experimental volumes of Kudoh and Takeuchi (1985), as expected of LDA calculated volumes.

Wadsleyite, like forsterite, is an orthorhombic crystal, having space group $Imma$. In Table 4 we compare lattice parameters and atomic positions of the relaxed structure at 0 GPa according to our calculations, with those experimentally obtained by Hazen et al. (2000). The level of agreement between both sets of results is comparable to that already observed in the case of forsterite

and that we will encounter again in subsequent structures. The spinel structure of Mg_2SiO_4 ringwoodite is cubic, with space group $Fd\bar{3}m$. Our relaxed structure has a lattice parameter of 8.13 Å at zero pressure, to be compared with the value of 8.071 Å reported by Hazen et al. (1993) (a difference of less than 1%). In this structure, the Mg atoms are found at Wyckoff positions 16d (1/2, 1/2, 1/2), while the Si atoms are at positions 8a (1/8, 1/8, 1/8). The oxygen atoms are found at 32e positions, with coordinates (x, x, x) . In our relaxation calculations, a value $x = 0.2443$ results, compared to the experimental value of $x = 0.2441$ reported by Hazen et al. (1993).

We now turn our attention to the structures with MgSiO_3 composition, starting with the perovskite structure. This polymorph presents an orthorhombic distortion with respect to the ideal cubic perovskite structure, which results from a concerted rotation of the SiO_6 octahedra present in the structure. In Table 5 we present a comparison of our calculated zero-pressure lattice parameters and atomic positions with experimental data at a similar pressure obtained by Ross and Hazen (1990). It can be appreciated there that once more the level of agreement in lattice parameters (differences smaller than 1%) falls within the expected range for the exchange-correlation functional used in this work, and is comparable to that obtained for the Mg_2SiO_4 polymorphs. To demonstrate that this is the case also at higher pressures, in Fig. 4 we plot a comparison of calculated and experimental lattice parameters and volume at a range of pressures. It can be seen there that the theoretical data mimics the response of the real system to the increasing pressure, as was the case for forsterite, discussed above. This is borne out by a comparison of the axial compressibilities; the experimental data provide values of β of 1.2, 1.0 and $1.2 \times 10^{-3} \text{ GPa}^{-1}$ for a , b and c , respectively, nearly identical to the theoretical values, namely 1.2, 1.1 and $1.2 \times 10^{-3} \text{ GPa}^{-1}$. It is interesting to note that here the compressibilities (both experimental and theoretical) along different crystallographic axes are very similar, contrary to what happens in the forsterite structure,

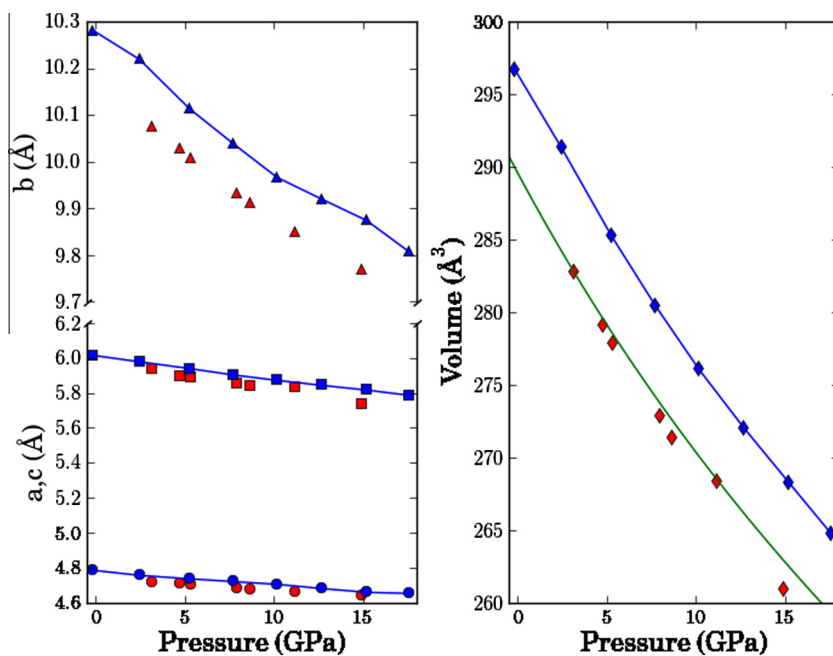


Fig. 3. Comparison of experimental and theoretical lattice parameters and volume vs. pressure for the forsterite structure. The experimental data, taken from Kudoh and Takeuchi (1985), is shown as red symbols, while the theoretical data from this work is shown as blue symbols with lines; parameters a , b and c are shown as circles, triangles and squares, respectively, while the volume is represented by diamonds. The scatter in the theoretical data, particularly noticeable in the b lattice parameter, is due to the relatively low sensitivity of the total energy to small changes in the lattice parameter values close to the equilibrium structure. As well as displaying experimental and calculated (this work) volume vs. pressure data, the right panel shows also a fit to the calculated data obtained by Li et al. (2007) at 300 K using the LDA approximation (continuous green line). (For interpretation of the references to colour in this figure legend, the reader is referred to the web version of this article.)

Table 4
Wadsleyite structural parameters at zero pressure. Experimental data are taken from Hazen et al. (2000).

Atom	Site	This work			Hazen et al. (2000)		
		a (Å)	b (Å)	c (Å)	a (Å)	b (Å)	c (Å)
		5.740	11.536	8.324	5.6978	11.4620	8.2571
		x	y	z	x	y	z
Mg	4a	0.0000	0.0000	0.0000	0.0000	0.0000	0.0000
Mg	4e	0.0000	0.2500	0.9706	0.0000	0.2500	0.9698
Mg	8g	0.2500	0.1274	0.2500	0.2500	0.1269	0.2500
Si	8h	0.0000	0.1196	0.6166	0.0000	0.1199	0.6165
O	4e	0.0000	0.2500	0.2167	0.0000	0.2500	0.2182
O	4e	0.0000	0.2500	0.7169	0.0000	0.2500	0.7157
O	8h	0.0000	0.9904	0.2554	0.0000	0.9898	0.2565
O	16j	0.2605	0.1226	0.9929	0.2601	0.1226	0.9931

Table 5
MgSiO₃, Perovskite structural parameters, as obtained from our structural relaxation calculations at zero pressure, compared to the experimental structure obtained by Ross and Hazen (1990) at room temperature and 0.001 GPa.

Atom	Site	This work			Ross and Hazen (1990)		
		a (Å)	b (Å)	c (Å)	a (Å)	b (Å)	c (Å)
		4.814	4.971	6.952	4.778	4.928	6.899
		x	y	z	x	y	z
Mg	4c	0.5147	0.5565	0.2500	0.5132	0.5563	0.2500
Si	4b	0.5000	0.0000	0.5000	0.5000	0.0000	0.5000
O	4c	0.1046	0.4645	0.2500	0.1031	0.4654	0.2500
O	8d	0.1961	0.2013	0.5540	0.1954	0.2011	0.5510

an observation that reflects the fact that the perovskite structure is more nearly isotropic. We also compare our results for the volume shown on the right panel of Fig. 4 to LDA values obtained by Karki et al. (2000) at 300 K. The green curve shown in the figure results from fitting the data of Karki et al. (2000) to a Birch-Murnaghan third order equation. It can be appreciated that their calculations

result in slightly lower volumes than those we obtain, as expected, but the volume response to imposed pressure is similar in both cases.

The remaining structures of MgSiO₃ composition relevant to this study are akimotoite and majorite. Akimotoite has the ilmenite structure (space group $R\bar{3}$), and majorite is a garnet; we have only considered the tetragonal $I4_1/a$ structure of majorite, with ordered cations. Tables 6 and 7 compare the structural parameters for these structures as obtained from our relaxation calculations with experimental data, and demonstrate they are reproduced with the same level of fidelity as obtained for the perovskite structure and for the structures of Mg₂SiO₄ composition considered above.

3.2. Vibrational properties

The calculation of phonon frequencies and related properties by means of the small-displacement method (Alfè, 2009) requires that the plane-wave cutoff be sufficiently large to adequately converge the forces on the atoms in the cell. We have checked that the kinetic energy cutoff of 500 eV used in our calculations was sufficient to comply with this requirement. Indeed, spot checks for the individual structures considered in this study show that the difference between atomic force components calculated with a kinetic energy cutoff of 500 eV and those obtained with a cutoff twice as large were of the order of 10^{-5} eV/Å, i.e. typically a factor of 10^4 smaller than the actual magnitude of the force components themselves. We thus performed all the phonon calculations reported below with the 500 eV plane-wave cutoff.

We will discuss in detail the calculation of vibrational frequencies and related properties for the particular cases of forsterite and the perovskite structures, as representatives of the Mg₂SiO₃ and MgSiO₃ stoichiometries, respectively. Calculated values for the remaining structures considered in this study will be provided in the appendix, but calculation procedures and analysis have been carried out in an entirely parallel fashion as for the cases of these representative structures. Nevertheless, in Figs. 5 and 6 we display

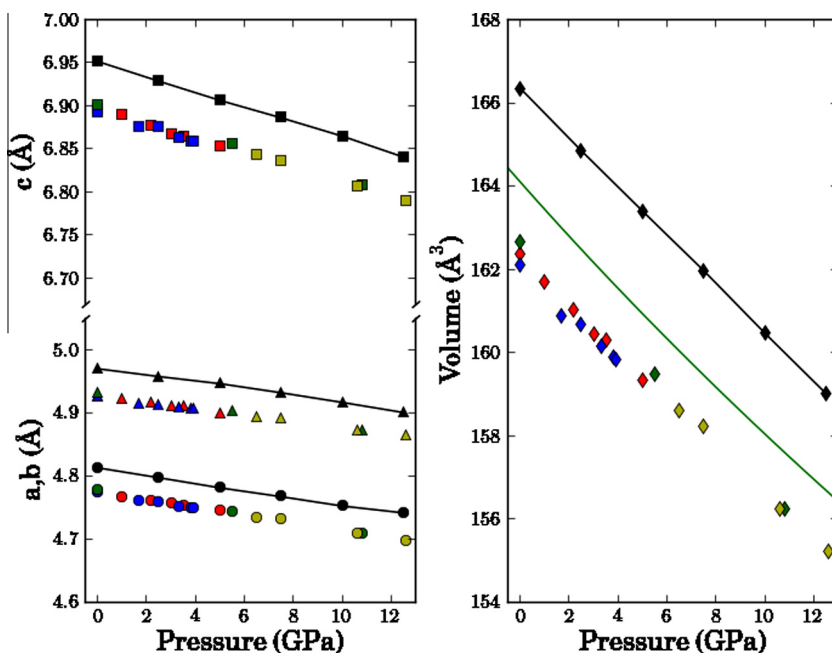


Fig. 4. Calculated and experimental lattice parameters and volume of the perovskite structure as a function of pressure. The experimental data is taken from Ross and Hazen (1990); different colours represent data from different samples. Our calculated data is shown as black symbols and continuous lines. The continuous green line shown on the right panel is a fit to the data obtained by Karki et al. (2000) using the LDA approximation. (For interpretation of the references to colour in this figure legend, the reader is referred to the web version of this article.)

Table 6

Structural parameters of akimotoite (ilmenite structure) obtained at 0 GPa; experimental results are taken from Yamanaka et al. (2005).

Atom	Site	This work			Yamanaka et al. (2005)		
		a (Å)	b (Å)	c (Å)	a (Å)	b (Å)	c (Å)
		4.785	4.785	13.670	4.729	4.729	13.559
		x	y	z	x	y	z
Mg	6c	0.0000	0.0000	0.36061	0.0000	0.0000	0.36029
Si	6c	0.0000	0.0000	0.1577	0.0000	0.0000	0.15773
O	18f	0.3217	0.03621	0.2404	0.3230	0.0366	0.23956

Table 7

Structural parameters of tetragonal majorite (space group $I4_1/a$). Experimental data is taken from Angel et al. (1989).

Atom	Site	This work			Angel et al. (1989)		
		a (Å)	c (Å)	$V(\text{Å}^3)$	a (Å)	c (Å)	$V(\text{Å}^3)$
		11.617	11.548	1558.5	11.501	11.480	1518.6
		x	y	z	x	y	z
Mg	8c	0.0000	0.0000	0.0000	0.0000	0.0000	0.0000
Mg	8e	0.5000	0.2500	0.6230	0.5000	0.2500	0.6258
Mg	16f	0.6294	0.0145	0.2690	0.6253	0.0112	0.2587
Si	4a	0.5000	0.2500	0.3750	0.5000	0.2500	0.3750
Si	4b	0.5000	0.2500	0.8750	0.5000	0.2500	0.8750
Si	8d	0.5000	0.0000	0.0000	0.5000	0.0000	0.0000
Si	16f	0.6249	0.0107	0.7560	0.6249	0.0065	0.7544
O	16f	0.5253	0.0586	0.6678	0.5282	0.0550	0.6633
O	16f	0.5439	0.9548	0.8605	0.5380	0.9529	0.8562
O	16f	0.7239	0.1060	0.8050	0.7195	0.1023	0.8021
O	16f	0.7129	0.9150	0.7021	0.7150	0.9106	0.7000
O	16f	0.4373	0.1628	0.4687	0.4412	0.1617	0.4680
O	16f	0.3977	0.2145	0.7824	0.3960	0.2080	0.7851

the calculated phonon band structures and corresponding densities of vibrational states for each of the structures considered here, calculated at 0 and 15 GPa. The high symmetry directions in the Brillouin zone used in the band structure plots correspond to those listed by Setyawan and Curtarolo (2010).

The forsterite structure has D_{2h} (mmm) point group symmetry, and its vibrational modes can thus be classified according to the irreducible representations of this point group. The primitive cell of this structure contains 28 atoms, giving rise to 84 vibrational modes, of which 3 will be acoustic modes having zero frequency at the Brillouin zone centre. Using group theory and with the help of program SAM (Kroumova et al., 2003) from the Bilbao Crystallographic server (Aroyo et al., 2006a,b, 2011) it is easy to see that the lattice vibrations of this structure can be decomposed into the following irreducible representations:

$$\Gamma_{vib} = 11A_g \oplus 10A_u \oplus 7B_{1g} \oplus 14B_{1u} \oplus 11B_{2g} \oplus 10B_{2u} \oplus 7B_{3g} \oplus 14B_{3u}. \quad (1)$$

For an orthorhombic structure such as forsterite, several choices of cell orientation are possible, which result from the different possible alignments of lattice vectors with symmetry elements. In this work we use the standard $Pnma$ setting (see above), but it is not infrequent to see forsterite described in the non-standard $Pbnm$ setting. While the actual choice of setting is of course physically irrelevant, it does affect the classification of the vibrational modes into irreducible representations of the space group. This should be borne in mind when comparing our data to that of previous calculations by other authors. Modes symmetric with respect to the inversion symmetry element of the structure (i.e. those pertaining to an irreducible representation with g sub-index) are Raman active, while those that are anti-symmetric (with a u sub-index) are Infrared (IR) active, with the

exception of modes having A_u symmetry, which are neither Raman nor IR active (silent modes). The three acoustic modes have $B_{1u} \oplus B_{2u} \oplus B_{3u}$ symmetries; the remaining 81 modes are optic. Bearing in mind all the above we can conclude that forsterite should have a total of 36 Raman-active modes and 38 IR-active modes (35 after excluding the three acoustic modes). In Table 8 we list the 0 GPa pressure calculated Raman mode frequencies. For comparison, we also list in the table the results of earlier theoretical calculations by Li et al. (2007) and Noel et al. (2006), as well as experimental results by Iishi (1978), Chopelas (1991a) and Gillet et al. (1991). Together with the phonon frequencies we list their pressure derivatives and Grüneisen parameter, $\gamma_i = -d \log v_i / d \log V$. Previous theoretical/experimental values for these are also provided when available. Also listed are the estimated frequencies at the experimental volume. Calculated values for the IR-active modes are listed in Table 9.

Let us first compare our results for the Raman active modes to the vibrational data obtained in previous theoretical studies, starting with that of Li et al. (2007). On average, our frequencies are $\sim 20 \text{ cm}^{-1}$ lower than their calculated values; lower frequencies are in better agreement, differing usually by less than 10 cm^{-1} , although the discrepancy increases with frequency, reaching $\sim 30 \text{ cm}^{-1}$ for the higher frequency modes. The fact that our calculated frequencies are smaller than the corresponding ones obtained by Li et al. (2007) is attributable in part to the fact that our calculated equilibrium volume (296.9 Å^3) is larger than the LDA predicted value, but also to the use of different exchange-correlation functionals (LDA in their case, GGA in ours). Since we have evaluated the phonon frequencies at a series of volumes, it is possible to estimate the frequencies that we would obtain at the LDA equilibrium volume, 289.5 Å^3 , according to Li et al. (2007). This exercise results in frequencies that agree with the LDA results much better than those listed in Tables 8 and 9, but still retaining an average mismatch of $\sim 10 \text{ cm}^{-1}$, which is thus likely to be attributable to the different functionals employed, as well as to other technical differences between the calculations (treatment of core electrons, etc). Li et al. (2007) also calculated the mode Grüneisen parameters, γ_i ; their reported values are in very good agreement with our own. There is overall good agreement between the LDA results of Li et al. (2007) and those obtained with the B3LYP hybrid functional by Noel et al. (2006), so much of what can be said about the comparison of our results with those of the former applies also to the comparison against the results of the latter.

Concerning the comparison with experimentally measured Raman spectra, on average our theoretical values are smaller by $\sim 25 \text{ cm}^{-1}$ than the corresponding frequencies reported by Iishi (1978) and those of Chopelas (1991a); agreement is also good with the values of Gillet et al. (1991), though the latter authors did not observe the complete series of Raman resonances. As in the comparison with other theoretical data in the previous paragraph, the agreement is better at low frequencies, and discrepancies increase with frequency. Likewise, a better comparison is achieved when we compare the experimental data with the theoretical frequencies interpolated at the experimental volume, reducing the average mismatch to about $\sim 15 \text{ cm}^{-1}$. It is worth noticing that this level of mismatch is not significantly larger than that existing between the different experimental reports. A second point of comparison is provided by the pressure derivatives of the mode frequencies and the mode Grüneisen parameters, $\gamma_i = -d \log v_i / d \log V$. Chopelas (1990) reported such data for a number of Raman-active modes (see Table 8), and the agreement between our calculated data for these parameters and their experimental values is reasonable; perhaps more important than the level of agreement itself is the fact that the observed trends are reproduced by the calculated values, i.e. oscillations in the experimental values of dv_i/dP and γ_i are reproduced by the calculated values.

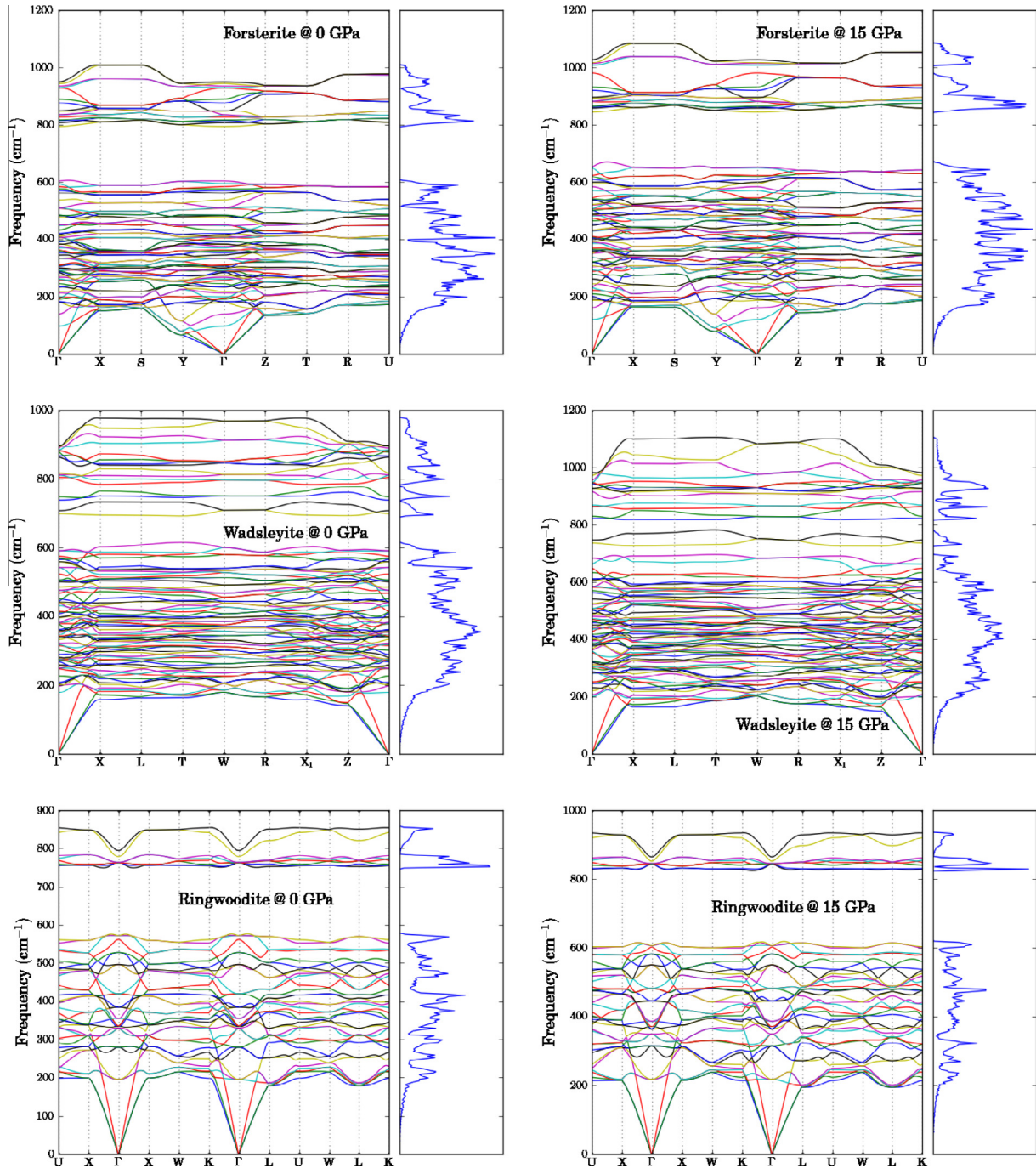


Fig. 5. Phonon band structures and vibrational densities of states at 0 and 15 GPa, calculated for the polymorphs of Mg_2SiO_4 stoichiometry.

With regard to the IR-active modes, let us first observe that we have not calculated the longitudinal-transversal splitting of IR optic modes (LO-TO splitting) expected in polar structures such as the ones considered here. The calculation of such splittings requires determining the Born effective charges for the chemical species involved, which we have not done. The LO-TO splitting is noticeable essentially at the centre of the Brillouin zone, and though it can be considerable for high frequency modes, its impact on the thermodynamic properties of the material is expected to be negligible (Alfè, 2009), since these result from an integration over the whole Brillouin zone, and the contribution to these properties of high frequency modes is reduced by the corresponding Boltzmann factor. The relevant comparison is thus between our data

and the TO-modes from previous theoretical or experimental studies. The appropriate data is listed in Table 9. There it can be seen that the level of agreement we find with the earlier theoretical results of Li et al. (2007) and Noel et al. (2006) is very similar as already found for the Raman active mode frequencies; on average, our calculated frequencies are smaller than the corresponding TO ones in those theoretical studies by an average of $\sim 20 \text{ cm}^{-1}$. The discrepancy is smallest (usually less than 10 cm^{-1}) in the low frequency range, and increases with frequency to an upper limit of $30\text{--}40 \text{ cm}^{-1}$. Comparison with experimental data reveals that there exists an average discrepancy of $\sim 25 \text{ cm}^{-1}$ (our frequencies being usually lower) with the IR data of Iishi (1978) and $\sim 30 \text{ cm}^{-1}$ with that of Hofmeister (1987). It should be noticed, however, that the

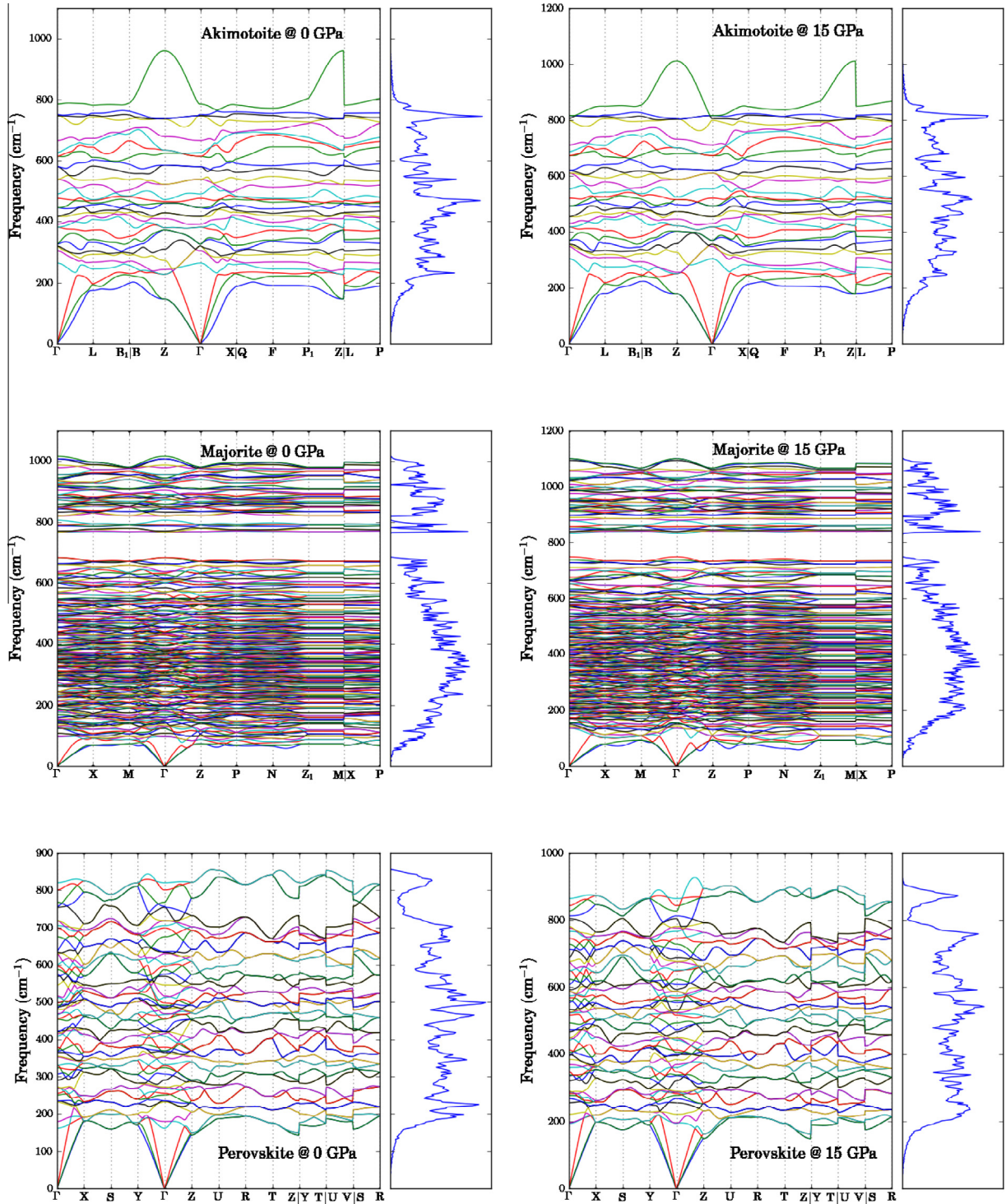


Fig. 6. Phonon band structures and vibrational densities of states at 0 and 15 GPa obtained for the MgSiO₃ polymorphs considered in this study.

correct assignment of experimental frequencies is not always obvious and in some particular cases it may be seen to be dubious (cases particularly noteworthy, where there is a consistent disagreement between all theoretical data and experiments, or even between different experimental results, are highlighted in Tables 8 and 9 by daggers on the experimental data). If it is borne in mind that the level of mismatch between different sets of experimental data is also in this range, we feel justified in considering our results to be in reasonable agreement with the empirical data.

The level of agreement between our calculated frequencies and experimental data can be better appreciated in Fig. 7, where we have plotted our theoretical frequencies in the pressure range 0–20 GPa. Raman-active mode frequencies are compared to the experimental data of Chopelas (1990), and IR modes to that of Wang et al. (1993). As already observed in Tables 8 and 9, the agreement is certainly not quantitative, neither in the magnitude of the frequencies nor in their pressure derivatives, but there is an overall agreement. The theoretical data displayed in Fig. 7 is

Table 8
Raman active modes of forsterite Mg_2SiO_4 . Frequencies are quoted in cm^{-1} , and their pressure derivatives in $\text{cm}^{-1} \text{GPa}^{-1}$. ν_i and $\nu_i(V_{\text{exp}})$ are calculated frequencies at the predicted $T = 0 \text{ K}$ equilibrium volume and at the experimental volume (Hazen, 1976), respectively. Our values are compared with the theoretical calculations of (a) Li et al. (2007) and (b) Noel et al. (2006), and experimental data is taken from (c) Iishi (1978), Chopelas (1991a), (e) Gillet et al. (1991) and (f) Chopelas (1990).

Mode symmetry	This work				Other theory		Experiment		
	ν_i	$\nu_i(V_{\text{exp}})$	$d\nu_i/dP$	γ_i	ν_i (a), (b)	γ_i (a)	ν_i (c), (d), (e)	$d\nu_i/dP$ (f)	γ_i (f)
B_{3g}	169	175	0.94	0.87	174, 183	0.09	142, 175, 171		
A_g	171	181	1.70	1.53	188, 188	0.30	183, 183, 183	3.03	2.09
B_{1g}	172	189	2.81	2.52	195, 190	1.11	226 [†] , 286 [†] , –		
B_{2g}	208	219	1.91	1.37	222, 225	0.81	192, 220, –		
A_g	212	220	1.36	0.92	222, 234	0.75	227, 226, 232	1.20	0.67
B_{3g}	224	243	3.11	2.03	249, 253	1.07	244, 242, 244	2.30	1.21
B_{2g}	237	251	2.38	1.48	256, 260	0.94	224, 274, –		
B_{1g}	278	292	2.27	1.16	284, 303	0.73	272, 315 [†] , –		
A_g	280	301	3.51	1.85	316, 307	1.21	305, 304, 307	3.90	1.63
B_{2g}	295	320	3.95	1.86	327, 317	1.20	260, 318, –		
B_{3g}	300	321	3.40	1.63	329, 324	1.24	324, 323, –		
A_g	302	326	3.86	1.81	333, 329	1.21	329, 329, 334	3.00	1.16
B_{1g}	302	321	3.00	1.39	320, 322	1.07	318, 374 [†] , 376 [†]		
B_{2g}	333	354	3.47	1.52	360, 367	1.16	318, 351, –		
A_g	334	360	4.05	1.64	357, 345	1.19	340, 339, 341	4.98	1.87
B_{3g}	348	365	2.83	1.13	370, 373	1.04	368, 365, –		
B_{1g}	353	374	3.42	1.40	383, 381	0.94	376, 410, 414	3.18	0.99
B_{2g}	353	374	3.30	1.28	384, 391	0.90	418 [†] , 383, –		
B_{1g}	399	425	4.15	1.35	418, 421	1.14	412, 435, 426	4.74	1.40
A_g	406	437	4.85	1.57	436, 425	1.36	424, 422, 426	4.75	1.43
B_{2g}	417	445	4.35	1.39	444, 442	1.23	434, 434, 443		
B_{3g}	426	459	5.19	1.58	450, 451	1.27	441, 439, –	5.50	1.60
A_g	516	530	2.16	0.55	529, 560	0.77	546, 545, 548	2.25	0.53
B_{2g}	540	564	3.70	0.93	569, 596	0.61	583, 582, 585		
B_{3g}	560	574	2.18	0.54	568, 608	0.57	588, 586, –	3.00	0.66
B_{1g}	568	584	2.50	0.61	577, 609	0.58	595, 592, 593		
A_g	577	598	3.24	0.76	596, 618	0.69	609, 608, 610	3.35	0.70
B_{2g}	594	618	3.71	0.86	618, 645	0.68	632, 632, –		
A_g	789	810	3.32	0.60	618, 645	0.68	632, 632, –		
B_{2g}	801	822	3.47	0.61	829, 835	0.48	839, 838, –		
B_{2g}	822	844	3.52	0.61	858, 866	0.40	866, 866, –		
A_g	827	845	3.04	0.53	850, 856	0.42	856, 856, 856	3.27	0.49
B_{3g}	846	865	3.03	0.50	877, 883	0.40	884, 881, 882	3.03	0.44
B_{1g}	888	906	2.79	0.44	914, 927	0.36	922, 920, 920	2.75	0.38
A_g	930	960	4.80	0.71	965, 967	0.59	966, 965, 967	4.99	0.66
B_{2g}	939	969	4.69	0.69	975, 979	0.59	976, 975, –		

that obtained at the predicted equilibrium volume; as already pointed out above, a slightly better match can be obtained by calculating the phonon frequencies at the experimental volume. In any case, it can be seen that calculated frequencies fall in the right range of values, and their pressure dependence is compatible with that of the observed experimental values.

Next, we consider the perovskite structure as representative of the phases with MgSiO_3 composition. In Tables 10 and 11 we list our calculated Raman and IR-active frequencies, respectively, together with their pressure-derivatives and Grüneisen parameters. Our data is once more compared to previous theoretical results, in this case as obtained by Karki et al. (2000) and Parlinski and Kawazoe (2000). We also compare our results to the available experimental data. The perovskite structure of MgSiO_3 is orthorhombic (space group $Pnma$, though frequently given in the non-standard setting of $Pbnm$). The atomic arrangement within the primitive unit cell of the structure has D_{2h} (mmm) point group symmetry. It contains 4 formula units, giving rise to 60 vibrational modes, 3 of which are acoustic, and the remaining ones optic. A symmetry analysis of the atomic displacements results in the following classification of the vibrational modes:

$$\Gamma_{\text{vib}} = 7A_g \oplus 8A_u \oplus 5B_{1g} \oplus 10B_{1u} \oplus 7B_{2g} \oplus 8B_{2u} \oplus 5B_{3g} \oplus 10B_{3u}, \quad (2)$$

of which the three acoustic modes transform according to irreducible representations $B_{1u} \oplus B_{2u} \oplus B_{3u}$. As occurred in the case of forsterite, symmetric modes with respect to inversion (i.e. A_g, B_{1g}, B_{2g} and B_{3g} modes) are Raman-active, while the antisymmetric ones are IR-active, with the exception of the A_u modes, which are silent. Thus there are a total of 24 Raman-active modes, and 25 optic IR-active modes. In practice, as we shall see, the number of modes actually observed in experiments is lower.

Comparing our phonon frequencies with previous predictions by Karki et al. (2000) and by Parlinski and Kawazoe (2000), both of whom used the LDA approximation, we can see that, as occurred in the case of forsterite, our results approach the LDA frequencies from below. The average discrepancy between our calculated frequencies and the LDA results is $\sim 20 \text{ cm}^{-1}$, both for the Raman and IR-active modes. Again, the agreement is better in the lower frequency range, and gradually deteriorates with increasing frequency (reaching values of $\sim 30 \text{ cm}^{-1}$), and much of the observed discrepancy is attributable to the difference in predicted equilibrium volumes. It is revealing to note that, even though the theoretical studies of Karki et al. (2000) and Parlinski and Kawazoe (2000) used the same LDA exchange-correlation functional, their results are not in perfect agreement with each other. Indeed, there is an average discrepancy of $\sim 15 \text{ cm}^{-1}$ between them, which is not that much smaller than the measured discrepancy to our own results,

Table 9

Infrared active modes of forsterite Mg_2SiO_4 . ν_i and $\nu_i(V_{\text{exp}})$ are calculated frequencies at the predicted $T = 0$ K equilibrium volume and at the experimental volume (Hazen, 1976), respectively. Only the transversal modes are given; frequencies are quoted in cm^{-1} , and their pressure derivatives in $\text{cm}^{-1} \text{GPa}^{-1}$. Our values are compared with the theoretical calculations of Li et al. (2007) (a) and Noel et al. (2006) (b), and experimental data is taken from Iishi (1978) (c), Hofmeister (1987) (d) and Wang et al. (1993) (e).

Mode symmetry	This work				Other theory		Experiment		
	ν_i	$\nu_i(V_{\text{exp}})$	$d\nu_i/dP$	γ_i	ν_i (a), (b)	γ_i (a)	ν_i (c), (d), (e)	$d\nu_i/dP$ (e)	γ_i (e)
B_{3u}	128	139	1.86	2.32	146, 143	1.06	144, 142		
B_{1u}	185	203	2.90	2.29	205, 206	1.16	201, 201		
B_{2u}	189	192	0.56	0.62	194, 207	0.63	201, 276 [†]		
B_{2u}	245	260	2.52	1.62	278, 278	0.57	224, 293		
B_{1u}	251	263	2.11	1.36	277, 275	0.57	224, 275		
B_{3u}	257	273	2.70	1.58	282, 277	0.80	224, 268		
B_{3u}	265	285	3.31	1.79	295, 292	0.74	280, 290		
B_{1u}	268	281	2.17	1.30	296, 294	1.04	274, 294		
B_{2u}	271	286	2.57	1.48	296, 290	0.81	274, 309		
B_{2u}	292	320	4.43	2.02	316, 313	1.11	296, 365		
B_{1u}	302	320	2.86	1.31	321, 322	1.12	293, 309		
B_{3u}	327	355	4.56	1.95	363, 350	1.27	294, 300		
B_{1u}	366	393	4.34	1.61	398, 388	1.13	320, 319 [†]		
B_{3u}	376	397	3.37	1.25	398, 403	1.11	352, 345		
B_{1u}	385	412	4.18	1.45	407, 412	1.07	378, 377		
B_{2u}	387	410	3.72	1.38	426, 420	1.24	365, 412		
B_{2u}	404	435	4.96	1.65	428, 428	1.38	423, 463		
B_{3u}	405	431	4.16	1.38	427, 432	1.20	400, 398		
B_{3u}	435	461	4.07	1.27	463, 465	1.14	421, 418		
B_{2u}	452	475	3.47	1.00	475, 490	0.96	483, 502		
B_{1u}	452	480	4.31	1.29	482, 476	1.00	403, 405 [†]		
B_{3u}	476	495	2.99	0.88	502, 517	0.74	465, 452		
B_{1u}	481	506	4.00	1.13	508, 513	0.89	498, 434		
B_{2u}	489	513	3.59	0.93	504, 514	0.87	502, 543, 517	2.02	0.50
B_{1u}	515	538	3.56	0.92	531, 540	0.86	562, 505		
B_{3u}	516	542	4.05	1.04	530, 535	0.86	510, 504		
B_{1u}	580	598	2.71	0.64	593, 614	0.61	601, 601		
B_{3u}	602	623	3.36	0.77	617, 638	0.66	537, 520, 614	2.57	0.54
B_{3u}	805	825	3.24	0.58	825, 835	0.48	838, 828		
B_{1u}	806	826	3.26	0.58	824, 838	0.48	838, 841, 846	2.58	0.39
B_{3u}	833	854	3.18	0.53	868, 870	0.43	882, 865		
B_{2u}	842	861	2.99	0.50	870, 874	0.40	885, 865, 887	2.71	0.39
B_{1u}	923	945	3.44	0.53	954, 962	0.41	957, 950, 962	2.38	0.32
B_{1u}	943	972	4.59	0.67	975, 982	0.61	980, 897		
B_{3u}	950	981	4.75	0.69	985, 989	0.59	987, 984, 992	5.01	0.65

obtained with a different functional. These differences should not be surprising, however. It should be observed that there are enough technical differences in the performance of the calculations to account for these small discrepancies, such as the fact that both studies used different implementations of DFT, obtained the phonon frequencies in different ways and accounted for core electrons differently. It can thus be seen that our calculated phonon frequencies are in good agreement with earlier theoretical results.

Let us now compare the calculated phonon frequencies against experimental data. Raman and IR spectra of MgSiO_3 perovskite have been published by a number of authors, but as already mentioned above, not all the active modes are actually detectable; this is particularly the case of the Raman data, where only up to 11 modes out of the expected 24 have been resolved in the experiments of Durben and Wolf (1992). In some other reports, such as that of Williams et al. (1987) only 4 peaks are clearly discernible. Theoretical calculations of Raman peak intensities in MgSiO_3 perovskite (Caracas and Cohen, 2006) have shown that peak intensities can vary over more than two orders of magnitude, and are sensitive to the excitation frequency employed and to other experimental factors. Thus it is not surprising that not all modes can be readily detected. The situation is slightly better in the case of IR data, but here also it is not infrequent for some modes to go undetected. Focusing on the Raman data first, we can see in Table 10 that the experimentally detectable modes are frequently A_g modes; while modes of other irreducible representations are sometimes

seen, they tend to have lower intensities. Our calculated frequencies are on average shifted down by some 20 cm^{-1} from the experimental values. Again, part of this discrepancy can be attributed to the difference in equilibrium volumes.

Table 11 lists, together with our calculated frequencies, experimental TO frequencies as reported by Lu et al. (1994) and Williams et al. (1987). The earlier study of Williams et al. (1987) only observed 4 frequencies, while Lu et al. (1994) detected 23 signals, only two short of the theoretical maximum of 25 IR-active modes allowed by symmetry (see above). However, out of these 23 modes, one has a reported frequency of 877 cm^{-1} , which seems to be significantly above any of the calculated frequencies in either this or previous theoretical studies (Karki et al., 2000; Parlinski and Kawazoe, 2000). Our highest IR frequency is calculated to be 767 cm^{-1} , to be compared with 781 and 809 cm^{-1} , as reported by Karki et al. (2000) and Parlinski and Kawazoe (2000), respectively. While there are discrepancies among the calculated highest frequencies, these remain within the expected bounds, and this leads us to suspect that the reported experimental mode frequency at 877 cm^{-1} may be due to an empirical artefact. Because the number of observed modes is lower than the calculated ones, it is not always possible to find an unambiguous correspondence between the two. This is particularly the case for the experimental modes falling in the range $450\text{--}700 \text{ cm}^{-1}$. So as to highlight that more than one correspondence between calculated and experimental data is possible,

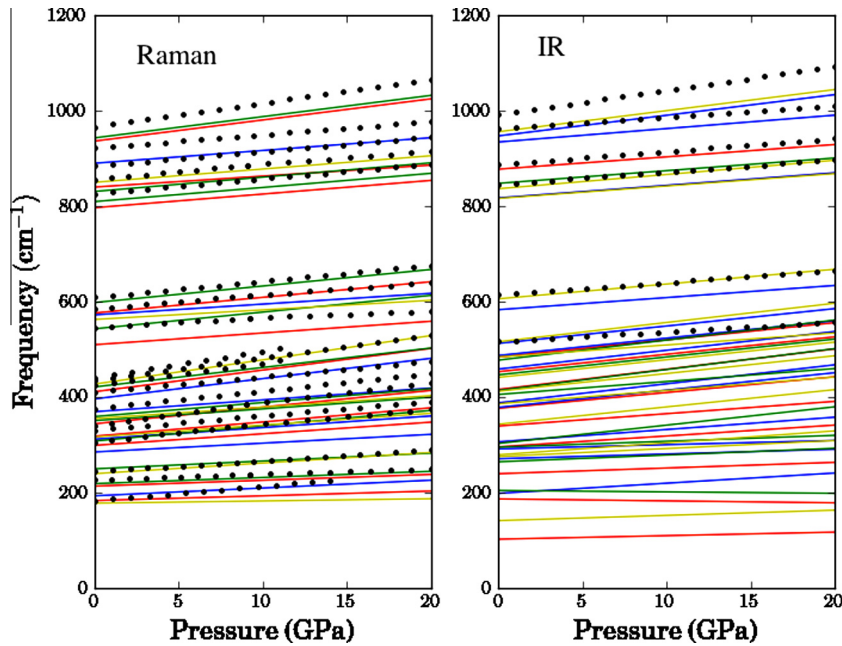


Fig. 7. Calculated Raman and infrared active phonon mode frequencies of forsterite vs. pressure. The left panel displays Raman active modes, A_g (red), B_{1g} (blue), B_{2g} (green) and B_{3g} (yellow); the black dots are obtained by interpolation from linear fits to the experimental Raman data of [Chopelas \(1990\)](#). In the right panel the frequencies of infrared-active modes are shown; A_u (red), B_{1u} (blue), B_{2u} (green) and B_{3u} (yellow); black dots are obtained from linear fits to the experimental data of [Wang et al. \(1993\)](#). (For interpretation of the references to colour in this figure legend, the reader is referred to the web version of this article.)

Table 10

Raman active modes of perovskite $MgSiO_3$. Frequencies are quoted in cm^{-1} , and their pressure derivatives in $cm^{-1} GPa^{-1}$. Our values are compared with the theoretical calculations of [Karki et al. \(2000\)](#) (a) and [Parlinski and Kawazoe \(2000\)](#) (b), and experimental data is taken from [Durben and Wolf \(1992\)](#) (c) and [Chopelas \(1996\)](#) (d).

Mode symmetry	This work				Other theory		Experiment		
	ν_i	$\nu_i(V_{exp})$	$d\nu_i/dP$	γ_i	ν_i (a), (b)	γ_i (a)	ν_i (c), (d)	$d\nu_i/dP$ (d)	γ_i (d)
A_g	209	219	1.14	3.01	234, 247	2.66	249, 245	2.01	2.14
B_{3g}	233	250	2.73	1.93	258, 230	2.39	254, 251	1.98	2.06
B_{1g}	258	275	2.54	2.15	277, 287	2.15			
A_g	265	277	1.83	1.58	281, 275	1.54	282, 279	1.49	1.39
B_{2g}	269	280	1.66	1.32	286, 266	1.23			
B_{2g}	315	327	2.04	1.09	331, 320	1.89	338, 327	1.77	1.41
B_{1g}	323	337	2.08	1.71	338, 345	1.15	343, 334	2.09	1.63
B_{2g}	352	367	2.39	1.35	376, 366	1.81	369, 370	1.50	1.06
A_g	365	381	2.73	1.13	380, 363	1.50	381, 379	1.76	1.21
A_g	376	394	2.74	1.76	400, 384	1.54	392, 387	1.99	1.34
B_{1g}	414	439	3.86	1.90	445, 429	2.00			
B_{3g}	417	434	2.89	0.84	438, 429	1.21			
A_g	475	501	4.01	1.72	518, 495	2.06	501, 499	3.44	1.80
B_{2g}	490	510	2.85	1.63	512, 492	1.26			
B_{3g}	490	525	5.61	2.05	518, 537	2.46			
B_{1g}	497	533	5.69	2.20	541, 544	2.33			
A_g	521	552	4.80	2.11	549, 558	1.86	542 ^d		
B_{2g}	599	622	3.56	1.44	616, 613	1.29			
B_{3g}	602	623	3.23	1.25	623, 619	1.21			
A_g	628	651	3.44	1.46	658, 648	1.29	666 ^d		
B_{2g}	637	660	3.54	1.37	660, 649	1.28			
B_{1g}	753	789	6.08	0.95	783, 819	1.35			
B_{2g}	790	817	4.00	1.28	827, 835	1.25			
B_{3g}	808	837	4.35	1.29	848, 855	1.32			

when necessary, we list the relevant empirical frequencies repeatedly in [Table 11](#). The pressure behaviour of the mode frequencies is displayed in [Fig. 8](#), where it is compared to the experimental data of [Chopelas \(1996\)](#) (Raman) and [Williams et al. \(1987\)](#) (IR data). As with the case of forsterite seen above, the agreement between calculated and experimental data in terms

of frequencies and pressure behaviour is not quantitative, but falls in line with what is expected from the computational methodologies that we have employed. This is true not only for the mode frequencies themselves, but is reflected also in their pressure derivatives and mode Grüneisen parameters (shown in [Tables 10 and 11](#)), as was also the case for forsterite.

Table 11

Infrared-active modes of perovskite MgSiO_3 . For completeness the silent A_u modes are also listed. Frequencies are quoted in cm^{-1} , and their pressure derivatives in $\text{cm}^{-1} \text{GPa}^{-1}$. Theoretical values by Karki et al. (2000) (a) and Parlinski and Kawazoe (2000) (b) are also listed. Experimental data is from references Lu et al. (1994) (c), Williams et al. (1987) (d) and Lu and Hofmeister (1994) (e). The assignment of experimentally measured frequencies to actual theoretical modes is not unambiguous; in such cases experimental frequencies have been listed more than once (see text).

Mode symmetry	This work				Other theory		Experiment	
	ν_i	$\nu_i(V_{\text{exp}})$	$d\nu_i/dP$	γ_i	ν_i (a), (b)	γ_i (a)	ν_i (c)	γ_i
B_{2u}	158	176	2.83	2.16	182, 157	3.05	180	
B_{3u}	230	243	2.01	1.78	251, 239	1.92	222	1.40 ^e
B_{1u}	247	262	2.32	1.80	272, 254	1.81	247	1.76 ^e
B_{2u}	288	304	2.37	1.66	309, 292	1.64	262	1.29 ^e
B_{1u}	301	319	2.62	1.91	326, 303	1.90	386	1.49 ^e
B_{3u}	327	348	3.18	1.90	348, 324	1.98	317	1.17 ^e
B_{3u}	364	385	3.17	1.72	391, 380	2.06	343	1.28 ^e
B_{3u}	408	425	2.71	0.99	422, 426	1.22	388	
B_{1u}	418	434	2.56	0.75	435, 434	1.08	415	
B_{2u}	419	448	5.06	0.59	446, 452	1.97	430	
B_{1u}	448	470	3.29	1.78	475, 458	1.87	444	
B_{2u}	459	488	4.60	1.76	486, 478	1.72	466, 484	
B_{3u}	464	489	3.97	1.78	504, 485	1.81	466, 484	
B_{1u}	487	515	4.36	2.04	511, 505	1.67	484, 496	
B_{3u}	508	533	3.73	1.86	549, 506	1.72	534	
B_{1u}	544	566	3.59	1.25	574, 566	1.54	534, 544 ^d	1.44 – 1.57 ^d
B_{2u}	559	576	2.60	1.24	598, 604	1.37	614, 614 ^d	
B_{1u}	564	584	2.91	1.71	597, 591	1.38	597	
B_{3u}	631	652	3.11	1.26	675, 606	1.39	679, 683 ^d	1.39 – 1.52 ^d
B_{2u}	671	705	5.23	1.92	710, 701	1.80	679, 683 ^d	1.15 – 1.29 ^d
B_{1u}	692	710	2.80	0.97	711, 722	0.93	705	
B_{2u}	699	731	4.80	1.79	723, 745	1.67	721	
B_{3u}	716	742	3.83	1.78	761, 748	0.96		
B_{1u}	749	779	4.52	1.60	776, 794	1.26	771	
B_{3u}	762	783	3.13	1.03	781, 809	1.52	780, 797 ^d	1.21 – 1.30 ^d
A_u	181	187	0.98	1.10	180 ^b			
A_u	252	267	2.28	2.02	253			
A_u	341	355	2.18	0.60	368			
A_u	369	382	2.12	0.86	383			
A_u	465	493	4.59	1.65	495			
A_u	582	604	3.49	1.03	617			
A_u	630	667	5.69	2.31	685			
A_u	712	744	4.91	1.74	763			

3.3. Theoretical phase diagrams of Mg_2SiO_4 and MgSiO_3

As detailed for the particular cases of forsterite and the perovskite structure of MgSiO_3 above, we have also computed the total energies and phonon frequencies of wadsleyite and ringwoodite (Mg_2SiO_4), and of akimotoite and majorite (MgSiO_3), together with those of MgO periclase and SiO_2 stishovite. This was done at a series of volumes approximately corresponding to a zero-temperature pressure range of ≈ -20 to 30 GPa. As noted above, in the interest of space we will not discuss the results obtained for the remaining structures here (numerical values of phonon frequencies, their pressure derivatives and Grüneisen parameters are provided in the appendix for structures wadsleyite, ringwoodite and akimotoite; those of majorite are listed in the accompanying [supplementary information file](#), where we also give plots of the vibrational band structures of MgO periclase and SiO_2 stishovite); suffice it to say that for all structures results were obtained of comparable quality to those of forsterite and the perovskite phase. This mass of data allows us to extend the zero-temperature phase diagram that can be deduced from the enthalpies of the various phases contemplated here, as seen in Fig. 2, to finite temperatures, by resorting to the quasi-harmonic approximation to the vibrational free energy. Let us first describe briefly our calculation procedure to do this.

As noted in Section 2, equilibrium volumes and relaxed configurations were determined for each structure at pressure intervals

corresponding to approximately 2.5 GPa in a pressure range of -20 to 30 GPa. At each volume the phonon frequencies were calculated as detailed above, over a dense grid of wave vectors spanning the 1st Brillouin zone. This allowed us to calculate the Helmholtz free energy within the quasi-harmonic approximation, as well as other thermal properties such as the entropy and constant volume heat capacity at each volume. The Helmholtz free energy of a defect-free lattice can be split as (Gillan et al., 2006):

$$F(T, V) = F_{\text{latt}}(T, V) + F_{\text{vib}}(T, V), \quad (3)$$

where F_{latt} is the free energy of the perfect (non-vibrating) lattice, and F_{vib} is the contribution due to the atomic dynamics. In the case of non-metallic systems, at temperatures at which electron excitations into conduction bands are negligible, the first term reduces to the total energy of the perfect lattice, which is then temperature-independent. All the systems considered in this study have sizeable gaps (see Section 2), and thus fall in this category. The second term can be easily estimated within the harmonic approximation, by viewing the dynamical lattice as an ensemble of harmonic oscillators, for which the free energy can be evaluated analytically as:

$$F_{\text{vib}}(T, V) \approx F_{\text{qh}}(V, T) = k_B T \sum_{n, \mathbf{k}} \ln \left[2 \sinh \left(\frac{\hbar \omega_{n\mathbf{k}}}{2k_B T} \right) \right], \quad (4)$$

where k_B is Boltzmann's constant, $\hbar = h/2\pi$, h being Planck's constant, and the sum extends over all vibrational modes and wave

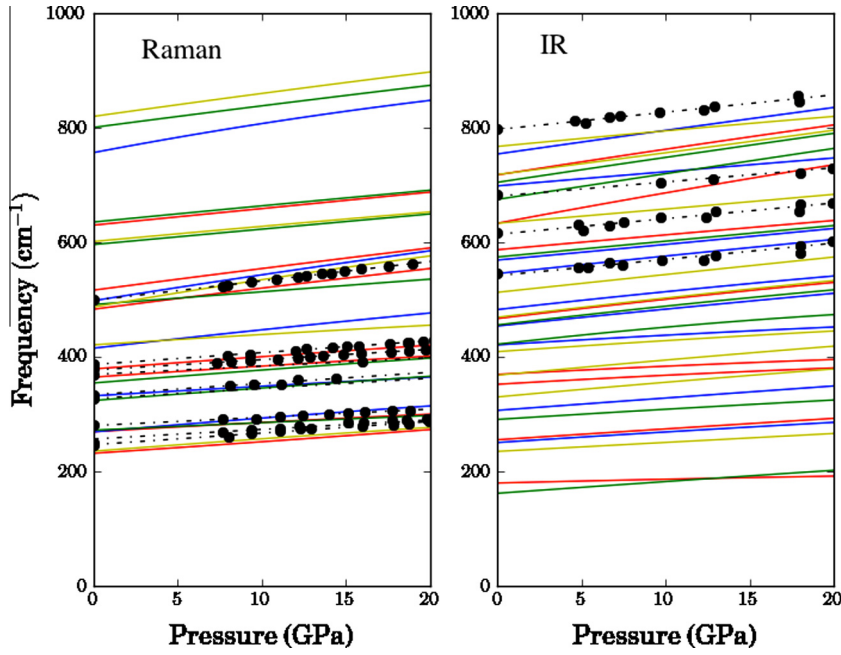


Fig. 8. Calculated Raman and infrared active phonon mode frequencies of MgSiO₃ perovskite vs. pressure. The left panel displays Raman active modes, A_g (red), B_{1g} (blue), B_{2g} (green) and B_{3g} (yellow); the black dots show experimental Raman data by [Chopelas \(1996\)](#), with the black dot-dash lines being linear interpolations to it. In the right panel the frequencies of infrared-active modes are shown; A_u (red), B_{1u} (blue), B_{2u} (green) and B_{3u} (yellow); black dots are obtained from the experimental data of [Williams et al. \(1987\)](#). (For interpretation of the references to colour in this figure legend, the reader is referred to the web version of this article.)

vectors within the 1st Brillouin zone. The neglect of anharmonicity is a reasonable approximation at low and moderate temperatures, but it is not valid close to the melting point, where anharmonicity effects make a substantial contribution to the free energy. The calculation of anharmonic corrections is possible, for example by resorting to thermodynamic integration techniques ([Hernández et al., 2007](#)), but we have not done so in this study. Eq. (4) can be further simplified when $\hbar\omega_{nk} \ll k_B T$, corresponding to the classical limit of the ensemble of harmonic oscillators, in which case we have:

$$F_{cl}(V, T) = k_B T \sum_{n,k} \ln \left(\frac{\hbar\omega_{nk}}{k_B T} \right). \quad (5)$$

Thus, our calculations of phonon frequencies in this study, together with Eqs. (4) [or (5) in the classical limit] allowed us to tabulate the Helmholtz free energy on a T-V grid for each structure considered in this study. From this it is straight-forward to obtain other thermal properties, such as the entropy, S , or pressure, P , given by

$$S(T, V) = - \left(\frac{\partial F}{\partial T} \right)_V, \quad (6)$$

$$P(T, V) = - \left(\frac{\partial F}{\partial V} \right)_T. \quad (7)$$

The latter expression contains a thermal contribution to the pressure coming from F_{vib} in Eq. (3). Evaluating $F(V, T)$ using Eqs. (3) and (4), and $P(T, V)$ according to Eq. (7), it is a straight-forward matter to compute the Gibbs free energy,

$$G(T, P) = F(T, V) + P(T, V)V, \quad (8)$$

which is actually the relevant thermodynamic potential required to analyse the stability of the various phases of a material in the temperature-pressure domain. At any given pressure and temperature, the thermodynamically stable phase is that having the lowest Gibbs free energy. Once the Gibbs free energy is available for each phase, there are other properties that become easily accessible, such as the specific heat, C_p , and the thermal expansion coefficient, α , which are

useful in order to gauge the degree of fidelity with which our computations reproduce the actual materials of relevance to this study.

In practice our numerical procedure was as follows: for each structure and volume, the Helmholtz free energy was tabulated on a thin temperature grid, ranging up to 3000 K, using Eqs. (3) and (4). Then, for every structure, $F(T, V)$ was fitted to a 5rd-order Chebyshev polynomial in V along the isotherms in the T-V grid. The behaviour of $F(T, V)$ was always very smooth, and such a polynomial expression was found to be perfectly adequate. From this fit $G(T, P)$ was derived using Eqs. (7) and (8), and tabulated over a T-P grid spanning the same temperature range as $F(T, V)$, and pressures from 0 to 30 GPa (in the low temperature limit). As noted above, from the tabulated $F(T, V)$ and $G(T, P)$ data, appropriately manipulated, it is possible to obtain the materials properties, such as the thermal expansion coefficient, α or the specific heat at constant pressure, C_p , defined respectively as

$$\alpha = \frac{1}{V} \left(\frac{\partial V}{\partial T} \right)_P, \quad (9)$$

$$C_p = \left(\frac{\partial H}{\partial T} \right)_P, \quad (10)$$

where $H = G(T, P) + ST$ is the enthalpy. These properties and a few others are presented in [Figs. 9 and 10](#), with numerical values at ambient conditions given in [Table 12](#), where they are compared against both results from other theoretical studies and experimental data. In fact this comparison provides an independent means through which to gauge the accuracy and reliability of our theoretical results. Specifically, [Table 12](#) lists values of α , the entropy S , and the specific heats (calculated at constant volume and constant pressure), evaluated at ambient conditions, namely $T = 300$ K and $P = 0$ GPa. The data shown in [Table 12](#) makes clear that there is a general consistency between the theoretical data. Small differences between calculated data exist; one discernible trend is that our calculated values for thermal expansion coefficient, entropy and specific heats tend to be slightly larger than those predicted by other functionals that result in smaller equilibrium volumes (LDA,

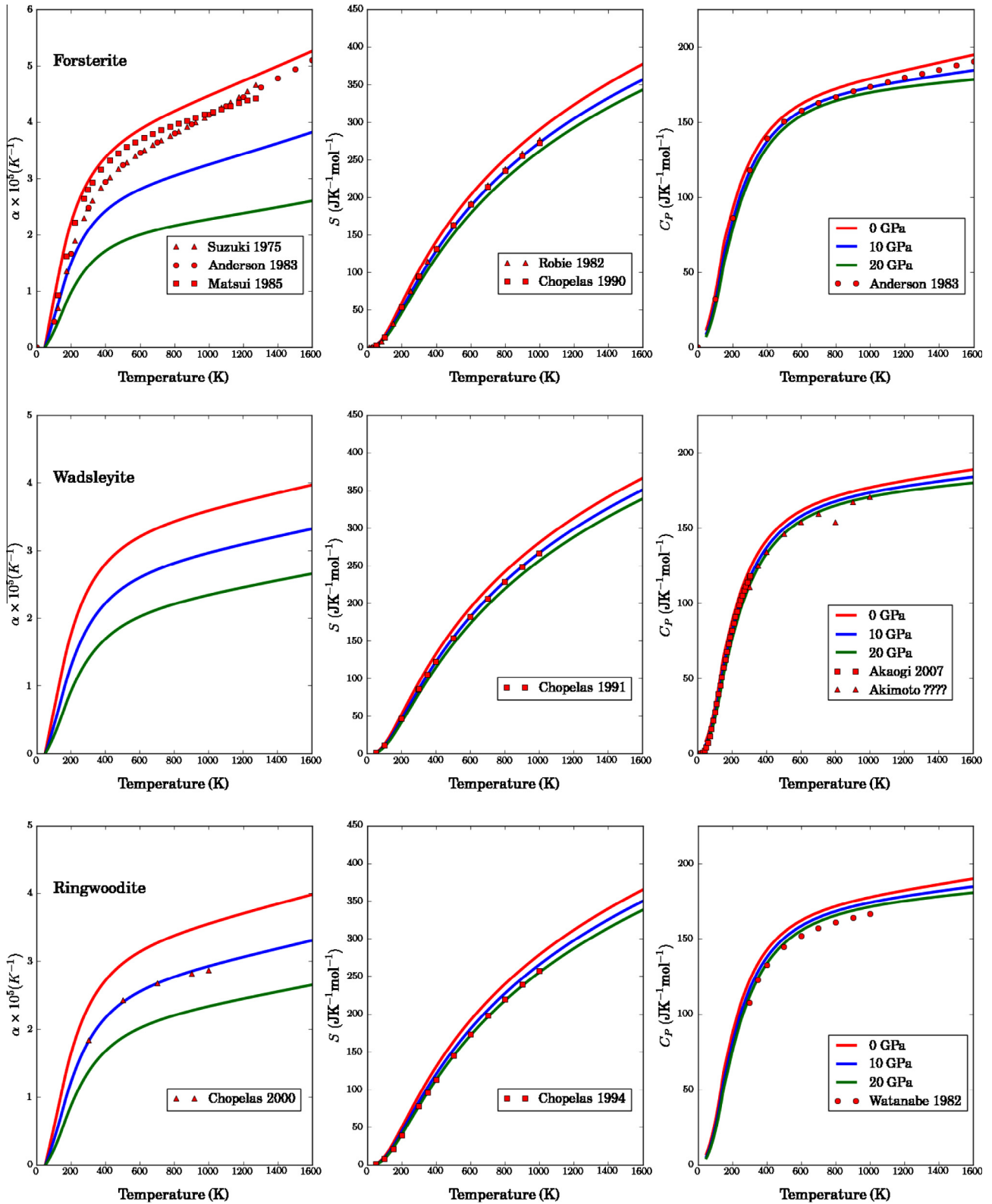


Fig. 9. Some thermal properties of the minerals with Mg_2SiO_4 composition vs. temperature at 0, 10 and 20 GPa pressure. Results are shown for the thermal expansion coefficient, α , the molar entropy, S and the specific heat at constant pressure, C_P . Experimental data is from Suzuki (1975), Anderson and Suzuki (1983), Matsui and Manghnani (1985), Chopelas (1990), Chopelas (1991b), Akaogi et al. (2007), Chopelas (2000), Chopelas et al. (1994) and Watanabe (1982).

B3LYP). But generally these differences are small. As regards comparison with the experimental data, let us first take the case of the thermal expansion. It can be seen that our theoretical values tend to be larger than the empirical ones, with differences that

sometimes reach $\sim 20\%$. We note however that the discrepancies between different experimental reports can also be of the same order of magnitude, and is not infrequent for the calculated values to fall within the range spanned by the experimental data (this

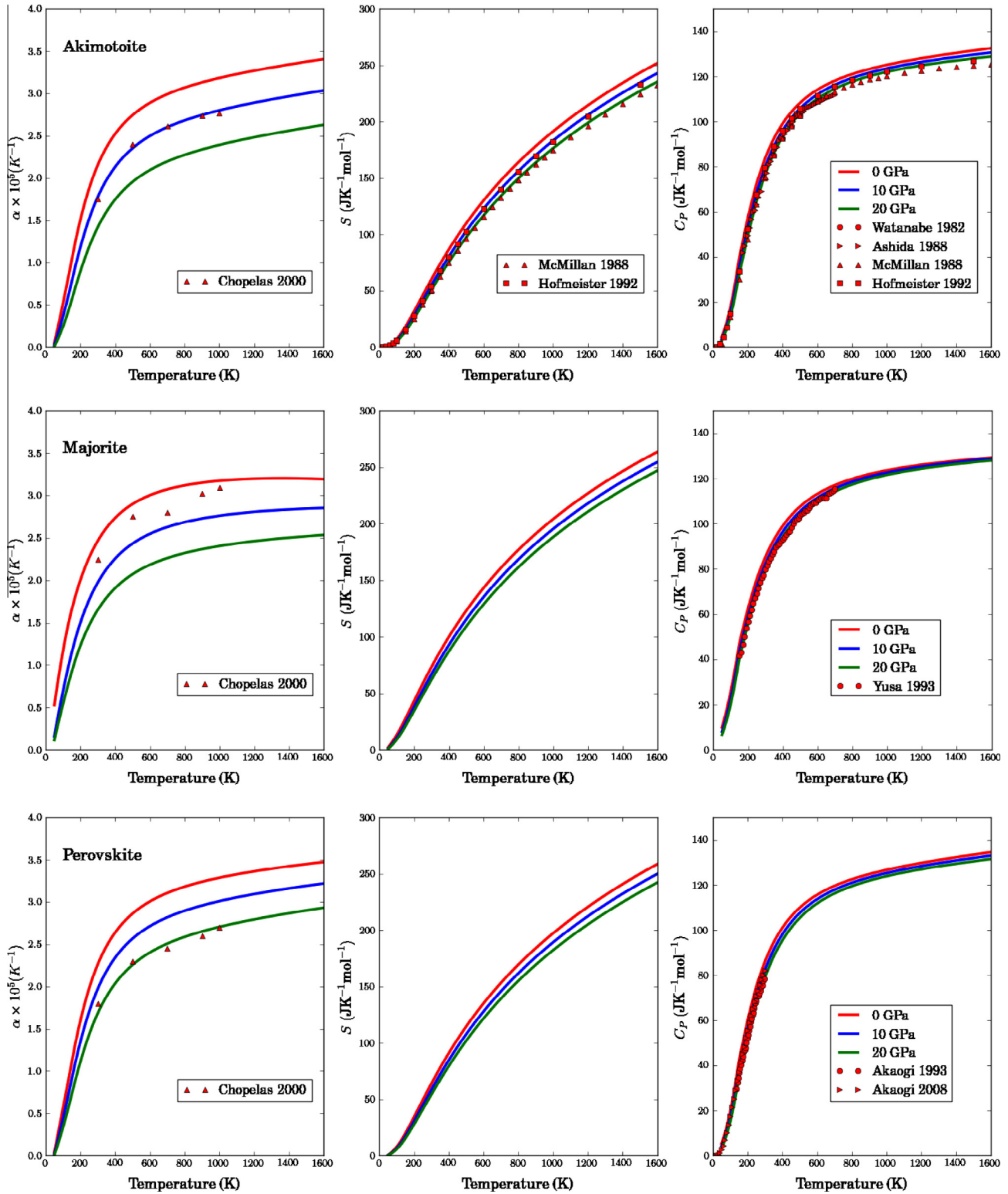


Fig. 10. Some thermal properties of the minerals with MgSiO_3 composition vs. temperature at 0, 10 and 20 GPa pressure. Results are shown for the thermal expansion coefficient, α , the molar entropy and the specific heat at constant pressure. Experimental data is from Chopelas (2000), McMillan and Ross (1988), Hofmeister and Ito (1992), Watanabe (1982), Ashida et al. (1988), Yusa et al. (1993), Akaogi and Ito (1993) and Akaogi et al. (2008).

occurs e.g. for *fo* and *wa*). A noticeable trend in the phases with Mg_2SiO_4 composition is that α diminishes along the *fo-wa-ri* sequence, i.e. α is smaller the higher the pressure at which the corresponding phase becomes stable. This trend is discernible both in the theoretical results as well as the experimental data.

As with the thermal expansion coefficients, our calculated entropies are also found to be larger (typically by $\sim 10\%$) than their measured counterparts. This is not surprising in view of the fact that our equilibrium volumes are also predicted to be larger. However, entropy differences between phases generally fall within the

Table 12

Some thermal properties of the different materials considered in this study. All properties have been evaluated at 300 K and 0 GPa on the basis of the quasi-harmonic approximation. α is the thermal expansion coefficient, S is the molar entropy, and C_v, C_p are the specific heat at constant volume and constant pressure, respectively. For each structure, the first row lists calculated results from this work and other theoretical studies, while the second row lists available experimental values. Calculated data reported by other authors: (a) [Ottonello et al. \(2009\)](#) (B3LYP); (b) [Li et al. \(2007\)](#) (LDA); (c) [Wu and Wentzcovitch \(2007\)](#) (LDA); (d) [Yu and Wentzcovitch \(2006\)](#) (LDA); (e) [Karki \(2002\)](#) (LDA); (f) [Karki et al. \(2000\)](#) (LDA); (g,h) [Yu et al. \(2011\)](#) (g LDA, h PBE); (i) [Karki et al. \(2000b\)](#) (LDA); (j) [Oganov et al. \(2005\)](#) (LDA). Experimental data is quoted from the following references: (k) [Chopelas \(1996\)](#) (l) [Chopelas \(2000\)](#) (m) [Kroll et al. \(2012\)](#), [Matsui and Manghnani \(1985\)](#) (o) [Trots et al. \(2012\)](#) (p) [Chopelas \(1990\)](#) (q) [Chopelas \(1991b\)](#), [Chopelas et al. \(1994\)](#), (s) [Akaogi et al. \(1984\)](#) (t) quoted by [Chopelas \(2000\)](#) from other sources; (u) [Robie et al. \(1982\)](#).

Structure	$\alpha \times 10^5$ (K ⁻¹)	S (JK ⁻¹ mol ⁻¹)	C_v (JK ⁻¹ mol ⁻¹)	C_p (JK ⁻¹ mol ⁻¹)
fo	2.93, 2.86 ^a , 2.64 ^b	101.3, 92.5 ^a , 95.9 ^b	120.50	122.65, 116.8 ^a , 119.3 ^b
	2.47 ^k , 2.6 ^m , 2.81 ⁿ , 3.23 ^o	94.29 ^p , 95.18 ^q , 95.85 ^u	116.4 ^r	116.21 ⁱ , 119.1 ^u
wa	2.51, 2.6 ^a , 2.21 ^c	93.40, 85.7 ^a , 88.67 ^c	119.00	122.21, 116.8 ^a , 118.1 ^c
	1.89 ^k , 2.14 – 2.34 ^o	85.87 ^q , 87.4 ^f	113.2 ^f	112.2 ^s
ri	1.90, 1.76 ^a , 1.97 ^d	88.90, 80.23 ^a , 85 ^d	119.41	120.57, 113.2 ^a , 116.9 ^d
	1.84 ^k	77.4 ± 0.6 ^r , 84.98 ^s	112.1 ^f	113 ± 0.3 ^r , 110.71 ^s
ak	2.13, 1.88 ^e , 1.92 ^h	59.50, 52.66 ^e	82.07, 80.1 ^h	83.19, 78.4 ^e , 82.7 ^h
	1.75 – 2.44 ^f		77.4 ^f	
mj	2.15, 2.5 ^g , 2.9 ^h	63.20	83.58	85.65, 83.0 ^g , 79.8 ^h
	2.24 ^f		79.9 ^f	
pv	2.25, 2.15 ^f , 2.19 ^h	63.20	83.58	85.65, 81.85 ^f , 82.61 ^h
	1.75 ^f	58.2 ± 0.3 ^k	81.9 ^f	82.7 ± 0.06 ^k
st	1.25	25.70, 26.81 ^j	42.24, 36.58 ^j	42.73
	1.36 ^f		41.4 ^f	
pe	3.41, 3.10 ^f	29.48, 26.65 ^s	37.64	38.63, 37.06 ^s
	2.79 – 3.10 ^k		36.4 ^f	

experimental error bounds, as can be appreciated in [Table 13](#), where we list the entropy and enthalpy differences at ambient conditions found in the Mg₂SiO₄ phases, comparing them to the calorimetric data of [Akaogi et al. \(2007\)](#). One exception to this rule is observed in the case of the wa-ri entropy difference, which we calculate to be -2.4 J/mol/K, a value which appears to be significantly smaller (in absolute value) than the experimental value of -3.7 ± 0.6 J/mol/K.

Having evaluated $G(T, P)$ [Eq. (8)] over a dense grid of T-P values as indicated above, determining the T-P phase diagram of Mg₂SiO₄ was then a simple matter of looping over all points in the T-P grid and checking, on each of them, which was the phase predicted to have the lowest Gibbs free energy value. Due to the different stoichiometries considered here, to the Gibbs free energies of akimotoite, majorite and the perovskite phase of MgSiO₃, that of periclase (MgO) at the same temperature and pressure conditions has to be added so as to make all phases chemically consistent. In the particular case of stishovite, it is necessary to add the Gibbs free energy of two formula units of MgO. We have thus obtained two phase diagrams for Mg₂SiO₄, one based on the full (quantum) quasi-harmonic approximation to the Helmholtz free energy [Eq. (4)], and a second one based on its classical limit [Eq. (5)]. Only the first is shown in [Fig. 11](#), as they are indistinguishable except at low temperatures. Altogether, six stability fields are displayed in the figure, corresponding to forsterite (green), wadsleyite (light blue), ringwoodite (purple), akimotoite plus periclase (red), perovskite plus periclase (dark blue), and stishovite plus periclase (yellow). The phase boundaries appear as white lines, and within each stability field the colour intensity increases in proportion to the free energy difference between the most stable phase and the second most stable phase. Contour lines (every 0.025 eV/f.u.) quantify the magnitude of such free energy differences. The small energy interval for the contour lines testifies to the difficulties involved in accurately determining stability fields and phase boundaries: indeed, small inaccuracies in relative free energies can considerably shift the position of a phase boundary in temperature and/or pressure. In constructing the phase diagram displayed in [Fig. 11](#) we have

for clarity omitted to include the data for phase majorite (plus periclase). Our results indicate that this phase would have a stability field coming down to ~2000 K, which would then wipe out the wadsleyite-perovskite-plus-periclase phase boundary and also the wadsleyite-ringwoodite-perovskite-plus-periclase triple point. Although a stability field of majorite-plus-periclase in this range of temperatures cannot be entirely ruled out, and one may indeed exist at slightly higher temperatures [see [Stixrude and Lithgow-Bertelloni \(2011\)](#)], we take the view that a stability field of majorite at temperatures as low as ~2000 K is probably an artefact due to the neglect of anharmonicity effects in this temperature range, or, perhaps more likely the result of neglecting the effects of cation disorder in the octahedral sites in this structure. Indeed, [Belmonte \(2013\)](#) has argued that small amounts of cationic disorder would be sufficient to significantly raise the stability field of majorite in temperature.

Excluding, as indicated above, the stability field of majorite plus periclase, the predicted phase diagram displayed in [Fig. 11](#) reproduces qualitatively the expected topology in the true phase diagram of Mg₂SiO₄, as deduced from experiments. At low temperatures the sequence of phases found as pressure is increased matches that found at zero temperature and obtained on the basis of enthalpy alone [see [Fig. 2](#)]. According to the data displayed in [Fig. 11](#), we can see that the ri-ak+pe-pv+pe triple point occurs at $T = 1565$ K and $P = 22.9$ GPa; a second triple point, between phases wa-ri-pv+pe, is predicted to occur at $T = 2452$ K and $P = 19.3$ GPa. The stability field of the st+pe combination is found to be rather small, extending only up to low temperatures. Indeed, as can be appreciated in [Fig. 11](#), a triple point between phases ak+pe-pv+pe-st+2pe is to be found approximately at $T = 125$ K, $P = 27.8$ GPa, and even at temperatures below this, the paleness of colour in the stability field of st+2pe indicates that this combination is not predicted to be strongly dominant anywhere in the phase diagram of Mg₂SiO₄.

The slopes of phase boundaries are of particular interest, as these are often estimated experimentally, thus providing a means to gauge the degree of accord between simulation predictions and

Table 13

Entropy and enthalpy differences at ambient conditions (298 K and 0 GPa) between the various phases of Mg_2SiO_4 considered in this study. Calorimetry results are quoted from Akaogi et al. (2007).

Transition	ΔS (J/mol/K)	ΔH (kJ/mol)
fo–wa this work	–8.2	30.2
exp.	-7.7 ± 0.4	27.2 ± 3.6
wa–ri this work	–2.4	12.3
exp.	-3.7 ± 0.6	12.9 ± 3.3
fo–ri this work	–10.6	42.5
exp.	-11.4 ± 0.5	40.1 ± 3.1

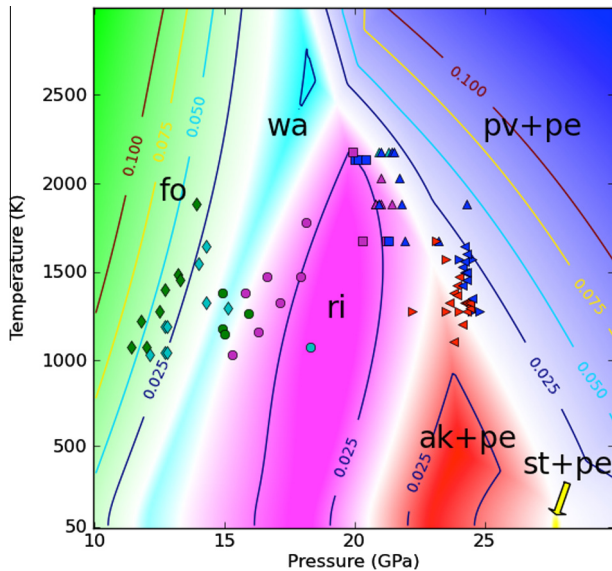


Fig. 11. Theoretical phase diagram of Mg_2SiO_4 . The colour coding is: green: forsterite; light blue: wadsleyite; purple: ringwoodite; red: akimotoite plus periclase; dark blue: perovskite plus periclase, and yellow: stishovite plus periclase. Phase boundaries are marked in white, and the intensity of colour within each stability field is proportional to the local free energy difference between the most stable and second most stable phase. Marked contour lines quantify this difference, in units of eV/f.u. Symbols represent experimental phase determinations carried out at temperature and pressure conditions indicated by the coordinates of each symbol, and are coloured according to the same code indicated above. Square symbols represent data from Katsura et al. (2003); circles, data from Suzuki et al. (2000); upward-pointing triangles, data from Fei et al. (2004); diamonds, data from Morishima et al. (1994); right-pointing triangles, data from Ito and Takahashi (1989), and left-pointing triangles, data from Ono et al. (2001). (For interpretation of the references to colour in this figure legend, the reader is referred to the web version of this article.)

experimental results. As can be seen in Fig. 11, the phase boundaries that result from our calculations are not simple straight lines, and thus do not have a constant slope. For example, the slope of the fo–wa coexistence line at $T = 1000$ K and $P = 13.8$ GPa is 2.4 MPa/K, while at $T = 1500$ K, $P = 14.9$ GPa it is 2.1 MPa/K. Experimentally determined slope values for this phase boundary range between 1.8 and 4 MPa/K (Akaogi et al., 1989; Katsura and Ito, 1989; Morishima et al., 1994; Katsura et al., 2004). Our own values fall towards the lower end of this range. Comparing to other theoretical calculations, Yu et al. (2008) obtained a slope value of 2.5 MPa/K, employing a similar computational approach to the one used here. This value is very close to the one we obtain at $T = 1500$ K. For the wa–ri phase transition we obtain slope values of 2.8 and 3 MPa/K at 1500 and 1700 K, respectively. These appear to be somewhat lower than the range of experimental values reported in the literature, 4.1–6.1 MPa/K (Suzuki et al., 2000; Inoue et al., 2006). A previous theoretical estimate by Yu et al.

(2008) (3.5 MPa/K) is more in line with our own, but still slightly larger than it.

The slope of the ri–pv+pe post-spinel transition is of great geophysical interest, as this phase transition is widely believed to be the main contributor to the seismic discontinuity marking the boundary between the transition zone and the lower mantle. Furthermore, the slope of this coexistence line could determine the nature of convection in the mantle (Christensen, 1995). A large slope would suggest that the 660 km discontinuity poses a significant barrier to global mantle convection. Conversely, a shallow slope would favour a global mantle convection model. At 1873 K we obtain a coexistence pressure of $P = 22.1$ GPa with a slope of -3.4 MPa/K. Averaging over the entire calculated coexistence line we obtain a mean slope value of -3.9 ± 1.3 MPa/K. Experimental estimations of the slope of this coexistence line seem to fall into two different ranges. Measurements by Ito and Takahashi (1989), Akaogi and Ito (1993), Irifune et al. (1998), Shim et al. (2001), Chudinovskikh and Boehler (2001) and Ye et al. (2014) favour values in the range -3 to -2.6 MPa/K. On the other hand, Katsura et al. (2003), Fei et al. (2004) and Litasov et al. (2005) favour values in the range -1.3 to -0.4 MPa/K. This apparent discrepancy among different empirical results testifies to the practical difficulties involved in extracting an accurate estimate of the slope when the phase boundary itself is insufficiently constrained. Our results tend to favour the larger (in absolute value) slope range, in agreement with previous theoretical results by Yu et al. (2007) (-2.9 MPa/K at 1900 K using GGA). As yet unpublished results from an all-electron B3LYP study by Belmonte (2013) find a value of -3.6 MPa/K, in very good agreement with our own value.

The slope of ri–pv+re post-spinel transition is also used in seismic studies to estimate the temperature anomalies associated with plumes and slabs. High temperatures would result in a shallow transition and the opposite for cold. Our results suggest that the deflection of the 660 km discontinuity should be as large or even greater than for the 410 km. Moreover, recent studies have seen

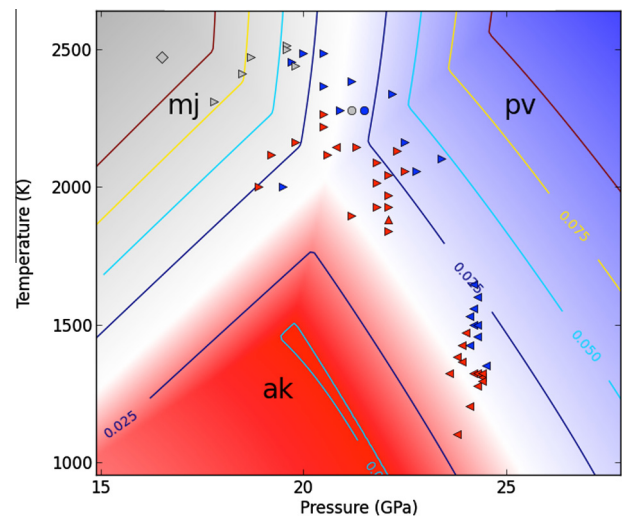


Fig. 12. Theoretical phase diagram of MgSiO_3 . The colour coding is: gray: majorite; red: akimotoite; blue: perovskite. Phase boundaries are marked in white, and the intensity of colour within each stability field is proportional to the local free energy difference between the most stable and second most stable phase. Marked contour lines quantify this difference, in units of eV/f.u. Symbols represent experimental phase determinations carried out at temperature and pressure conditions indicated by the coordinates of each symbol, and are coloured according to the same code indicated above. The diamond is from Presnall et al. (1998); circles, data from Hirose et al. (2001); upward-pointing triangles, data from Fei et al. (2004); left-pointing triangles, data from Ono et al. (2001), and right-pointing triangles, data from Chudinovskikh and Boehler (2001). (For interpretation of the references to colour in this figure legend, the reader is referred to the web version of this article.)

deflections on the order of 34 km or so Day and Deuss (2013). If our large slope is correct, this can be the result of an anomaly of only 350 K. The much lower slope of 1 MPa/K found in some studies would require unrealistic temperature anomalies of over 1000 K.

For the ilmenite-perovskite transition we obtain a mean slope of -3.5 ± 0.8 MPa/K, averaged over the whole ak+pe–pv+pe phase boundary. Closer to the ri–ak+pe–pv+pe triple point the slope increases (in absolute value) to values comparable to those of the ri–pv+pe coexistence line, i.e. ~ -4 MPa/K. This transition has been investigated experimentally by Ito and Takahashi (1989), who extracted a slope estimate of -2.5 MPa/K. Later, Ono et al. (2001) reported a slope of -2.9 ± 2 MPa/K using Au as the pressure standard, and a value of -3.5 ± 2.4 MPa/K using the Pt pressure standard. Similar experiments were conducted by Hirose et al. (2001), who reported a slope estimate of -2.7 MPa/K. Chudinovskikh and Boehler (2004) have obtained a slope of -4 ± 0.2 MPa/K using diamond-anvil cell measurements. Our result falls closer to the more negative values found by Ono et al. (2001) and by Chudinovskikh and Boehler (2004), but is not incompatible with the less negative ones found by other authors, and falls within the range of experimentally reported values. Yu et al. (2011) calculate a steeper Clapeyron slope of -6 ± 1 MPa/K for this transition.

We are not aware of any previous experimental report on the ri–ak+pe phase boundary and its slope. Contrary to the cases of wa–pv+pe and ri–pv+pe boundaries, where the slope is found to be negative, the slope of the ri–ak+pe phase boundary is positive, with an average value of 1.65 ± 0.6 MPa/K. Yu et al. (2011) have estimated a Clapeyron slope of 1.2 MPa/K for this transition, which is slightly shallower than ours but falls within our estimated error bars for this slope.

Finally, in Fig. 12 we illustrate the phase diagram of MgSiO₃ in the neighbourhood of the mj–ak–pv triple point. This phase diagram has been calculated from the same data and following the same procedure as for that of Mg₂SiO₄ [see Fig. 11], but considering only the relevant MgSiO₃ phases. According to our results, the mj–ak–pv triple point is located at 20.5 GPa and 2040 K. This value is reasonably close to that quoted by Hirose et al. (2001), 20 GPa and 2193 K. On the other hand, Yu et al. (2011) calculate the position of the triple point to be 21.8 GPa and 1840 K using a similar computational procedure to the one we have employed, while Belmonte (2013) using an all-electron B3LYP calculation locate it at 21.09 ± 0.13 GPa and 2247 ± 31 K. We calculate the value of the slope of the mj–pv boundary to be 1.1 MPa/K. This value is in very good agreement with that of a previous theoretical calculation by Yu et al. (2011) (1.2 ± 0.3 MPa/K using a GGA functional); it is

Table A.14

Raman-active vibrational modes of wadsleyite. Frequencies are given in (cm⁻¹), and their pressure derivatives in (cm⁻¹ GPa⁻¹). The third column lists data interpolated at the experimental volume quoted by Hazen et al. (2000). Other theoretical data is quoted from Wu and Wentzcovitch (2007). The experimental data is from Chopelas (1991b). Tentative mode assignments are based on best matchings between calculated data at the experimental equilibrium volume and experimental frequencies.

Mode symmetry	This work				Other theory			Experiment		
	ν_i	$\nu_i(V_{exp})$	$d\nu_i/dP$	γ_i	ν_i	γ_i	ν_i	$d\nu_i/dP$	γ_i	
B_{2g}	194	197	1.06	0.68	201	0.60	199			
B_{1g}	207	217	4.03	2.25	230	1.69	214	2.1	1.7	
B_{3g}	220	226	2.39	1.27	232	1.34	231	1.68	1.25	
A_g	249	258	3.52	1.65	267	1.48	252	1.18	0.81	
B_{1g}	251	260	2.53	1.42	264	1.66	262	1.80	1.19	
B_{3g}	263	269	2.46	0.99	275	0.69	273	1.40	0.88	
B_{2g}	264	270	1.52	0.91	270	1.04				
A_g	275	282	1.90	1.02	285	1.18	279	1.02	0.63	
B_{3g}	285	295	2.51	1.31	303	1.59	297			
B_{1g}	286	295	1.90	1.04	297	1.18	311	1.60	0.89	
B_{2g}	312	325	3.38	1.56	334	1.66	326	3.02	1.59	
A_g	330	341	2.74	1.24	344	1.34	341	2.68	1.36	
B_{1g}	339	350	3.10	1.25	360	1.34	360			
B_{3g}	343	357	3.09	1.47	361	1.41				
B_{2g}	349	358	3.11	1.09	367	1.45	370	1.58	0.74	
B_{1g}	361	379	3.73	1.71	386	1.82	382	3.48	1.58	
B_{2g}	377	398	3.69	1.78	400	1.82	398	3.15	1.37	
B_{3g}	382	395	3.02	1.25	401	1.62				
A_g	386	400	3.91	1.39	406	1.58				
B_{3g}	413	425	2.51	0.98	425	1.08	426	2.40	0.97	
A_g	420	431	3.68	1.25	424	1.39	443	3.47	1.35	
A_g	431	447	3.65	1.32	455	1.29				
B_{1g}	435	448	1.68	0.87	448	0.94	460			
B_{3g}	465	477	3.43	0.95	482	0.96				
B_{2g}	473	484	2.46	0.85	484	0.92	491	1.95	0.69	
B_{3g}	509	529	4.77	1.47	544	1.34				
A_g	542	560	5.35	1.33	557	1.32	553	4.31	1.34	
B_{2g}	554	563	2.66	0.65	564	0.75				
B_{3g}	564	582	3.09	1.01	578	1.02	580	3.50	1.04	
B_{2g}	589	613	4.62	1.38	625	1.51	610			
A_g	607	618	4.46	0.99	607	0.77	620	2.48	0.69	
A_g	692	710	3.49	0.80	712	0.91	723	3.37	0.80	
B_{3g}	747	770	5.31	1.13	786	1.16	778	4.83	1.07	
B_{3g}	803	822	4.42	0.86	829	0.92	812			
A_g	849	873	5.21	1.02	895	1.02	845	3.98	0.81	
B_{1g}	854	877	5.43	0.97	891	1.05	885			
B_{2g}	872	895	5.47	0.95	914	0.99				
A_g	882	902	4.22	0.76	911	0.91				
B_{3g}	893	917	5.40	0.96	935	0.98	919	4.40	0.83	

Table A.15

Infrared-active vibrational modes in wadsleyite. The A_u modes (7 in total) are silent, and have been listed separately. There are 13 B_{1u} modes, 12 B_{2u} modes and 10 B_{3u} modes. Other theoretical data is quoted from [Wu and Wentzcovitch \(2007\)](#). Experimental data is quoted from [Cynn and Hofmeister \(1994\)](#).

Mode symmetry	This work				Other theory		Experiment		
	ν_i	$\nu_i(V_{exp})$	$d\nu_i/dP$	γ_i	ν_i	γ_i	ν_i	$d\nu_i/dP$	γ_i
B_{3u}	173	180	2.45	1.59	191	1.24	192	0.46	0.41
B_{2u}	194	202	3.89	2.19	216	1.47	210	0.18	0.15
B_{3u}	247	248	0.99	0.23	252	0.17	265	0.00	0.00
B_{1u}	247	256	3.44	1.56	267	1.33			
B_{1u}	275	285	4.76	1.84	300	1.41	290	2.13	1.26
B_{2u}	275	281	2.11	0.92	285	1.30			
B_{3u}	280	288	2.63	1.26	295	1.26			
B_{2u}	302	307	2.05	0.78	313	0.84	315	2.29	1.30
B_{3u}	314	324	3.19	1.38	332	1.62			
B_{1u}	326	336	4.08	1.44	354	1.58	336		
B_{2u}	340	354	3.59	1.53	359	1.44	345		
B_{1u}	341	358	3.77	1.71	358	1.37			
B_{3u}	343	355	2.86	1.22	359	1.40			
B_{1u}	357	375	3.16	1.61	380	1.75	375		
B_{3u}	389	407	3.01	1.44	411	1.51	407		
B_{2u}	401	418	4.07	1.57	427	1.50			
B_{1u}	410	425	3.80	1.33	431	1.54			
B_{2u}	437	452	3.09	1.16	455	1.20	461	2.67	0.96
B_{2u}	446	460	2.85	1.08	462	1.05			
B_{1u}	452	468	3.83	1.29	469	1.32			
B_{3u}	462	481	4.34	1.42	488	1.26			
B_{1u}	479	493	2.54	0.96	498	1.11	501	1.51	0.52
B_{2u}	498	513	2.93	0.98	514	1.07	513	2.79	0.93
B_{3u}	507	524	4.25	1.25	535	1.25			
B_{3u}	525	547	3.22	1.26	551	1.18	541	3.6	1.13
B_{1u}	547	561	5.57	1.24	553	1.23			
B_{2u}	557	581	5.35	1.50	590	1.26	584	2.99	0.86
B_{1u}	585	595	3.57	0.82	587	1.09			
B_{1u}	675	695	4.56	1.05	699	1.16	690	4.06	1.00
B_{2u}	756	779	5.23	1.10	794	1.14	760		
B_{2u}	806	825	4.39	0.87	833	0.94			
B_{1u}	838	860	5.00	0.98	872	0.98	868		
B_{1u}	873	895	5.08	0.91	910	0.93	890	4.10	0.77
B_{2u}	906	929	4.68	0.89	947	0.94	935	4.91	0.90
B_{3u}	882	903	4.94	0.87	918	0.96			
A_u	205	209	1.63	0.93					
A_u	264	276	3.15	1.67					
A_u	355	369	3.12	1.40					
A_u	374	386	2.86	1.17					
A_u	539	549	2.38	0.68					
A_u	876	898	5.30	0.92					

also in good agreement with the experimental value determined by [Hirose et al. \(2001\)](#) (1.3 MPa/K). As for the mj-ak phase boundary, this is calculated to have a slope of 7.2 MPa/K, a value which is in very good agreement with that previously reported by [Yu et al. \(2011\)](#), who found a value of 7.4 ± 0.5 MPa/K.

4. Summary and conclusions

We have conducted a thorough computational study of the relative stability of various geophysically relevant phases of $MgSiO_3$ and Mg_2SiO_4 composition. Total energies and relaxed structures have been obtained on the basis of DFT calculations. Harmonic phonon frequencies have been obtained and classified for each structure at a range of volumes, and quasi-harmonic free energies have been derived from them. The Gibbs free energy for each phase has been tabulated on a fine temperature-pressure grid spanning the range of environmental conditions relevant to the bottom of the upper mantle, the transition zone and the top of the lower mantle. While the quasi-harmonic treatment is expected to break down at high temperatures, it is nevertheless expected to provide a qualitatively correct picture of the phase diagrams. The actual location of phase boundaries is very sensitive to relative errors in the free energies, but the slopes of coexistence lines are expected to be more robust. Our calculated phase diagrams for Mg_2SiO_4

and $MgSiO_3$ seem to reproduce the major features of the corresponding phase diagrams obtained from experimental measurements and thermodynamic models ([Stixrude and Lithgow-Bertelloni, 2011](#)), and is also in general good agreement with theoretical results obtained previously for individual coexistence lines ([Wentzcovitch et al., 2010](#) and refs. therein).

Acknowledgements

The authors wish to acknowledge Dr. M. Amman, Prof. D. Dobson and Prof. L. Stixrude for enlightening discussions. ERH thanks the Leverhulme Trust for the award of a Leverhulme Visiting Professorship to UCL, during which this work was started, and the Spanish Research and Innovation Office through project No. FIS2012-31713. Calculations were performed in the UCL ISD Research Computing cluster Legion.

Appendix A. Vibrational properties of Wadsleyite

Wadsleyite has an orthorhombic structure with space group $Imma$. The arrangement of atoms within the primitive cell has point group symmetry D_{2h} (mmm). Using this information, together with the data reported in [Table 4](#), the lattice phonons at the zone

Table B.16

Ringwoodite vibrational modes symmetric with respect to inversion. The A_{1g}, E_g (doubly degenerate) and T_{2g} (triply degenerate) modes are Raman active; the T_{1g} (triply degenerate) mode is silent (Raman and IR inactive). Frequencies are given in (cm^{-1}), and their pressure derivative in ($\text{cm}^{-1} \text{GPa}^{-1}$). The second column, headed by $\nu_i(V_{exp})$, gives the frequency of the corresponding mode interpolated at the experimental volume given by Hazen et al. (1993) (see Table 2). Other theoretical results are quoted from Yu and Wentzcovitch (2006) (a) and Piekarz et al. (2002) (b); experimental data is from references Chopelas et al. (1994) (c) and McMillan and Akaogi (1987) (d).

Mode symmetry	This work				Other theory		Experiment	
	ν_i	$\nu_i(V_{exp})$	$d\nu_i/dP$	γ_i	ν_i (a)	ν_i (b)	ν_i (c)	ν_i (d)
T_{2g}	281	292	2.88	1.68	309	282	302	302
T_{1g}	329	339	2.43	1.23		317		
E_g	357	366	2.43	1.12	375	343	372	370
T_{2g}	574	584	2.65	0.75	586	571	600	600
T_{2g}	765	789	6.37	1.37	817	778	796	794
A_{1g}	795	816	5.33	1.11	831	805	834	836

centre can be decomposed into the following irreducible representations:

$$\Gamma_{wa} = 11A_g \oplus 7A_u \oplus 7B_{1g} \oplus 14B_{1u} \oplus 9B_{2g} \oplus 13B_{2u} \oplus 12B_{3g} \oplus 11B_{3u}. \quad (\text{A.1})$$

This translates into a total of 39 Raman active modes (A_g, B_{1g}, B_{2g} and B_{3g}), and 38 infrared active modes (B_{1u}, B_{2u} and B_{3u}), including the three acoustic modes, with species $B_{1u} \oplus B_{2u} \oplus B_{3u}$. The A_u modes are silent.

Tables A.14 and A.15 list our calculated Raman-active and IR-active mode frequencies, respectively. The data is presented following a similar pattern to that used for the cases of forsterite and the perovskite structures (see text). Comparison is presented with both previous theoretical calculations and experimental data.

Appendix B. Vibrational properties of Ringwoodite

The spinel structure of ringwoodite has space group $Fd\bar{3}m$. As discussed in the text, Mg ions occupy $16d$ Wyckoff positions, with Si ions located at $8a$ and oxygens at $32e$ positions. The primitive cell of such an atomic arrangement has point group symmetry $O_h(m\bar{3}m)$, and applying a group theoretical analysis to such a structure results in the following mechanical representation:

$$\Gamma_{ri} = A_{1g} \oplus 2A_{2u} \oplus E_g \oplus 2E_u \oplus T_{1g} \oplus 5T_{1u} \oplus 3T_{2g} \oplus 2T_{2u}, \quad (\text{B.1})$$

of which the A_{1g}, E_g and T_{2g} modes are Raman active, while the T_{1u} modes are IR active; one of the latter modes is acoustic. The remaining modes (T_{1g}, A_{2u}, E_u and T_{2u}) are silent. The increased symmetry in this structure as compared to those of forsterite and wadsleyite

results in a number of degeneracies; indeed modes of irreducible species $E_{g(u)}$ are doubly degenerate, while those of species $T_{1(2)g(u)}$ are triply degenerate.

Our calculated phonon frequencies for ringwoodite are listed in Tables B.16 (inversion-symmetric modes) and B.17 (antisymmetric modes). Comparison with previous calculation results and experimental data is also provided.

Appendix C. Vibrational properties of Akimotoite

The ilmenite structure of akimotoite has space group $R\bar{3}$, with Mg and Si cations occupying $6c$ sites, and oxygens located at the general $18f$ positions. The point group symmetry of the primitive cell of this structure is $C_{3i}(-3)$. A group analysis of this structure results in the following mechanical representation:

$$\Gamma_{ak} = 5A_g \oplus 5A_u \oplus 5E_g \oplus 5E_u. \quad (\text{C.1})$$

Discounting the three acoustic modes, of species $A_u \oplus E_u$, this structure has a total of 18 optical modes, of which 9 are doubly degenerate ($5E_g \oplus 4E_u$). The inversion-symmetric g modes are Raman active, while antisymmetric u ones are IR active. Raman and IR active modes are listed in Tables C.18 and C.19, respectively, where our results are compared to existing theoretical and experimental data from the literature.

Appendix D. Vibrational properties of Majorite

The majorite structure has space group $I4_1/a$ with Mg cations occupying Wyckoff sites $8c, 8e$ and $16f$; Si cations are found at posi-

Table B.17

Inversion antisymmetric vibrational modes in ringwoodite. The triply-degenerate T_{1u} modes are infrared active; the remaining modes are silent. Frequencies are given in (cm^{-1}), and their pressure derivative in ($\text{cm}^{-1} \text{GPa}^{-1}$). The second column, headed by $\nu_i(V_{exp})$, gives the frequency of the corresponding mode interpolated at the experimental volume given by Hazen et al. (1993) (see Table 2). Theoretical results by other authors are quoted from refs. (a) Yu and Wentzcovitch (2006) and (b) Piekarz et al. (2002); experimental results are from (c) Akaogi et al. (1984), where some of the signals were described as *shoulder* (sh) or *weak* (w).

Mode symmetry	This work				Other theory		Experiment
	ν_i	$\nu_i(V_{exp})$	$d\nu_i/dP$	γ_i	ν_i (a)	ν_i (b)	ν_i (c)
T_{2u}	194	206	3.43	3.47		223	
T_{1u}	333	342	2.82	1.26	345	350	350(w)
E_u	335	348	4.12	1.99		355	
T_{1u}	389	404	3.75	1.64	423	396	395(sh), 445
T_{2u}	421	437	4.11	1.66		407	
T_{1u}	502	515	3.83	1.26	549	475	510(sh), 545(w)
E_u	531	546	3.62	1.15		523	
A_{2u}	560	572	3.25	0.95		563	
T_{1u}	768	791	6.01	1.30	829	761	785(sh), 830
A_{2u}	781	801	5.37	1.14		790	

Table C.18

Raman-active modes in ilmenite Akimotoite. Frequencies are in (cm^{-1}), and their pressure derivative in ($\text{cm}^{-1} \text{GPa}^{-1}$). LDA calculated data is from Karki (2002). Experimental data is quoted from Reynard and Rubie (1996).

Mode symmetry	This work				Other theory		Experiment		
	ν_i	$\nu_i(V_{exp})$	$d\nu_i/dP$	γ_i	ν_i	γ_i	ν_i	$d\nu_i/dP$	γ_i
A_g	268	286	2.40	1.94	294	1.92	294	2.1	1.60
E_g	326	339	1.74	1.18	343	1.15	351	1.7	1.10
E_g	383	400	2.22	1.24	400	1.32	402	2.2	1.24
A_g	391	406	1.96	1.10	414	1.02	413	2.3	1.26
E_g	458	478	2.73	1.27	488	1.25	484	2.7	1.24
A_g	476	496	2.67	1.19	490	1.27	499	3.1	1.40
E_g	583	601	2.47	0.92	614	0.85	620	2.4	0.88
A_g	644	672	3.62	1.20	680	1.18	680	3.3	1.10
A_g	756	784	3.74	1.06	783	1.09	798	3.7	1.04
E_g	762	794	4.32	1.21	795	1.24			

Table C.19

Infrared-active modes in ilmenite akimotoite. Frequencies are in (cm^{-1}), and their pressure derivative in ($\text{cm}^{-1} \text{GPa}^{-1}$). LDA calculated data is from Karki (2002). Experimentally determined frequency ranges are as given by Hofmeister and Ito (1992).

Mode symmetry	This work				Other theory		Experiment
	ν_i	$\nu_i(V_{exp})$	$d\nu_i/dP$	γ_i	ν_i	γ_i	ν_i
A_u	304	325	2.81	2.00	330	1.93	384–421
E_u	317	340	3.05	2.03	346	2.07	337–364
E_u	419	435	2.15	1.11	439	1.06	450–482
A_u	485	514	3.87	1.68	509	1.74	526–552
E_u	554	585	4.15	1.59	595	1.54	623–642
E_u	621	651	3.86	1.31	648	1.33	670–820
A_u	683	703	2.65	0.84	702	0.79	735–820
A_u	759	783	3.16	0.90	768	1.00	

tions 4a, 4b, 8d and 16f while oxygen anions are located at six different 16f orbits. The primitive cell contains a total of 80 atoms, and has point group symmetry $C_{4h}(4/m)$. The mechanical representation of this structure is

$$\Gamma_{mj} = 25A_g \oplus 34A_u \oplus 27B_g \oplus 31B_u \oplus 28E_g \oplus 34E_u. \quad (\text{D.1})$$

Of these, the modes with E species are doubly degenerate. The A_g , B_g and E_g modes are Raman active, while the A_u and E_u modes are IR active; B_u modes are silent. The three acoustic modes pertain to irreducible species A_u and E_u ; the remaining modes are optic. The large number of vibrational modes in this structure (237 optical modes) makes impractical their full listing here; nevertheless we provide a listing of all modes, together with their pressure derivative and Grüneisen parameters, in the supplementary information file that accompanies this paper.

Appendix E. Supplementary data

Supplementary data associated with this article can be found, in the online version, at <http://dx.doi.org/10.1016/j.pepi.2014.10.007>.

References

- Akaogi, M., Ito, E., 1993. Heat capacity of MgSiO_3 perovskite. *Geophys. Res. Lett.* 20, 105.
- Akaogi, M., Ito, E., Navrotsky, A., 1989. Olivine?modified spinel?spinel transitions in the system Mg_2SiO_4 ? – Fe_2SiO_4 : Calorimetric measurements, thermochemical calculation, and geophysical application. *J. Geophys. Res.: Solid Earth* 94 (B11), 15671–15685.
- Akaogi, M., Kojitani, H., Morita, T., Kawaji, H., Atake, T., 2008. Low-temperature heat capacities, entropies and high-pressure phase relations of MgSiO_3 ilmenite and perovskite. *Phys. Chem. Miner.* 35 (5), 287–297.
- Akaogi, M., Ross, N.L., McMillan, P.F., Navrotsky, A., 1984. The Mg_2SiO_4 polymorphs (olivine, modified spinel and spinel): thermodynamic properties from oxide melt solution calorimetry, phase relations, and models of lattice vibrations. *Am. Miner.* 69 (5–6), 499–512.
- Akaogi, M., Takayama, H., Kojitani, H., Kawaji, H., Atake, T., 2007. Low-temperature heat capacities, entropies and enthalpies of Mg_2SiO_4 polymorphs, and $\alpha/\beta/\gamma$

- and post-spinel phase relations at high pressure. *Phys. Chem. Miner.* 34 (3), 169–183.
- Alfè, D., 1999. Ab initio molecular dynamics, a simple algorithm for charge extrapolation. *Comput. Phys. Commun.* 118, 31–33.
- Alfè, D., 2009. Phon: a program to calculate phonons using the small displacement method. *Comput. Phys. Commun.* 180 (12), 2622–2633.
- Anderson, O.L., Suzuki, I., 1983. Anharmonicity of three minerals at high temperature: forsterite, fayalite, and periclase. *J. Geophys. Res.: Solid Earth* 88, 3549.
- Angel, R.J., Finger, L., Hazen, R.M., Kanzaki, M., Weidner, D.J., Liebermann, R., Veblen, D., 1989. Structure and Twinning of single-crystal MgSiO_3 Garnet Synthesized at 17 GPa and 180 °C.
- Aroyo, M.I., Perez-Mato, J.M., Orobengoa, D., Tasci, E., de la Flor, G., Kirov, A., 2011. Crystallography online: Bilbao crystallographic server. *Bulgarian Chem. Commun.* 43 (2), 183–197.
- Aroyo, M.I., Perez-Mato, J.M., Capillas, C., Kroumova, E., Ivantchev, S., Madariaga, G., Kirov, A., Wondratschek, H., 2006b. Bilbao crystallographic server I: databases and crystallographic computing programs. *Z. Krist.* 221, 15–27.
- Aroyo, M.I., Kirov, A., Capillas, C., Perez-Mato, J.M., Wondratschek, H., 2006a. Bilbao crystallographic server II: representations of crystallographic point groups and space groups. *Acta Cryst.* A62, 1150128.
- Ashida, T., Kume, S., Ito, E., Navrotsky, A., 1988. MgSiO_3 Ilmenite: heat capacity, thermal expansivity, and enthalpy of transformation. *Phys. Chem. Miner.* 16, 239.
- Becke, A.D., 1993. Density-functional thermochemistry. III. the role of exact exchange. *J. Chem. Phys.* 98 (5648–5652).
- Belmonte, D., Sep 2013. Ab initio Thermodynamics of Deep Mantle Minerals: The System MgO-SiO_2 . Unpublished Ph.D Thesis, University of Genova.
- Bina, C.R., Helffrich, G., 1994. Phase transition Clapeyron slopes and transition zone seismic discontinuity topography. *J. Geophys. Res.* 99, 15853.
- Birch, F., 1947. Finite elastic strain of cubic crystals. *Phys. Rev.* 71 (11), 809–824.
- Blöchl, P.E., 1994. Projector augmented-wave method. *Phys. Rev. B* 50, 17953–17979.
- Caracas, R., Cohen, R.E., 2006. Theoretical determination of the Raman spectra of MgSiO_3 perovskite and post-perovskite at high pressure. *Geophys. Res. Lett.* 33.
- Chopelas, A., 1990. Thermal properties of forsterite at mantle pressures derived from vibrational spectroscopy. *Phys. Chem. Miner.* 17, 149.
- Chopelas, A., 1991a. Single crystal raman spectra of forsterite, fayalite and monticellite. *Am. Miner.* 76, 1101–1109.
- Chopelas, A., 1991b. Thermal properties of β – Mg_2SiO_4 at mantle pressures derived from vibrational spectroscopy: implications for the mantle at 400 km depth. *J. Geophys. Res.: Solid Earth* 96, 11817.
- Chopelas, A., 1996. Thermal expansivity of lower mantle phases MgO and MgSiO_3 perovskite at high pressure derived from vibrational spectroscopy. *Phys. Earth Planet. In.* 98, 3–15.

- Chopelas, A., 2000. Thermal expansivity of mantle relevant magnesium silicates derived from vibrational spectroscopy at high pressure. *Am. Miner.* 85 (2), 270–278.
- Chopelas, A., Boehler, R., Ko, T., 1994. Thermodynamics and behavior of γ – Mg_2SiO_4 at high pressure: implications for Mg_2SiO_4 phase equilibrium. *Phys. Chem. Miner.* 21, 351.
- Christensen, U., 1995. Effects of phase transitions on mantle convection. *Annu. Rev. Earth Planet. Sci.* 23, 65.
- Chudinovskikh, L., Boehler, R., 2001. High-pressure polymorphs of olivine and the 660-km seismic discontinuity. *Nature* 411, 574.
- Chudinovskikh, L., Boehler, R., 2004. MgSiO_3 phase boundaries measured in the laser-heated diamond cell. *Earth Planet. Sci. Lett.* 219, 285.
- Cynn, H., Hofmeister, A.M., 1994. High-pressure IR spectra of lattice modes and OH vibrations in Fe-bearing wadsleyite. *J. Geophys. Res.: Solid Earth* 99, 17717–17727.
- Day, E.A., Deuss, A., 2013. Reconciling PP and P'P' precursor observations of a complex 660 km seismic discontinuity. *Geophys. J. Int.* 194, 834–838.
- Durben, D.J., Wolf, G.H., 1992. High-temperature behavior of metastable MgSiO_3 perovskite: a Raman spectroscopic study. *Am. Miner.* 77, 890–893.
- Fei, Y., Orman, J.V., Li, J., van Westrenen, W., Sanloup, C., Minarik, W., Hirose, K., Komabayashi, T., Walter, M., Funakoshi, K.-I., 2004. Experimentally determined postspinel transformation boundary in Mg_2SiO_4 using MgO as an internal pressure standard and its geophysical implications. *J. Geophys. Res.* 109 (B2), B02305.
- Gillan, M.J., Alfè, D., Brodholt, J., Vocadlo, L., Price, G.D., 2006. First-principles Modelling of Earth and Planetary Materials at High Pressures and Temperatures.
- Gillet, P., Richet, P., Guyot, F., Fiquet, G., 1991. High-temperature thermodynamic properties of forsterite. *J. Geophys. Res.: Solid Earth* 96 (B7), 11805–11816.
- Hazen, R.M., 1976. Effects of temperature and pressure on the crystal structure of forsterite. *Am. Miner.* 61, 1280–1293.
- Hazen, R.M., Downs, R., Finger, L., Ko, J., 1993. Crystal chemistry of ferromagnesian silicate spinels: Evidence for Mg-Si disorder. *Am. Miner.* 78, 1320–1323.
- Hazen, R.M., Weinberger, M., Yang, H., Prewitt, C.T., 2000. Comparative high-pressure crystal chemistry of wadsleyite, β – $(\text{Mg}, \text{Fe})_2\text{SiO}_4$ with $x = 0$ and 0.25. *Am. Miner.* 85, 770–777.
- Hernández, E.R., Antonelli, A., Colombo, L., Ordejón, P., 2007. The calculation of free-energies in semiconductors: defects, transitions and phase diagrams. In: Drabold, D.A., Estreicher, S.K. (Eds.), *Theory of Defects in Semiconductors*. Springer-Verlag, Berlin.
- Hirose, K., Komabayashi, T., Murakami, M., Funakoshi, K.-I., 2001. In situ measurements of the majorite-akimotoite-perovskite phase transition boundaries in MgSiO_3 . *Geophys. Res. Lett.* 28 (23), 4351–4354.
- Hofmeister, A.M., 1987. Single-crystal absorption and reflection infrared spectroscopy of forsterite and fayalite. *Phys. Chem. Miner.* 14 (6), 499–513.
- Hofmeister, A.M., Ito, E., 1992. Thermodynamic properties of MgSiO_3 ilmenite from vibrational spectra. *Phys. Chem. Miner.* 18, 423.
- Hohenberg, P., Kohn, W., 1964. Inhomogeneous electron gas. *Phys. Rev.* 136, 864.
- Iishi, K., 1978. Lattice dynamics of forsterite. *Am. Miner.* 63, 1198–1208.
- Inoue, T., Irifune, T., Higo, Y., Sanehira, T., Sueda, Y., Yamada, A., Shinmei, T., Yamazaki, D., Ando, J., Funakoshi, K., Utsumi, W., 2006. The phase boundary between wadsleyite and ringwoodite in Mg_2SiO_4 determined by in situ X-ray diffraction. *Phys. Chem. Miner.* 33 (2), 106–114.
- Irifune, T., Nishiyama, N., Kuroda, K., Inoue, T., Isshiki, M., Utsumi, W., Funakoshi, K.-I., Urakawa, S., Uchida, T., Katsura, T., Ohtaka, O., 1998. The postspinel phase boundary in Mg_2SiO_4 determined by in situ X-ray diffraction. *Science* 279, 1698.
- Ito, E., Takahashi, E., 1989. Postspinel transformations in the system Mg_2SiO_4 – Fe_2SiO_4 and some geophysical implications. *J. Geophys. Res.* 94, 10637.
- Jacobsen, S.D., Holl, C.M., Adams, K.A., Fischer, R.A., Martin, E.S., Bina, C.R., Lin, J.-F., Prakapenka, V.B., Kubo, A., Dera, P., 2008. Compression of single-crystal magnesium oxide to 118 GPa and a ruby pressure gauge for helium pressure media. *Am. Miner.* 93 (11–12), 1823–1828.
- Karki, B.B., 2002. First-principles lattice dynamics and thermoelasticity of MgSiO_3 ilmenite at high pressure. *J. Geophys. Res.* 107 (B11), 2267.
- Karki, B.B., Wentzcovitch, R.M., de Gironcoli, S., Baroni, S., 2000. Ab initio lattice dynamics of MgSiO_3 perovskite at high pressure. *Phys. Rev. B (Condens. Matter Phys.)* 62, 83792.
- Karki, B.B., Wentzcovitch, R.M., de Gironcoli, S., Baroni, S., 2000b. High-pressure lattice dynamics and thermoelasticity of MgO. *Phys. Rev. B (Condens. Matter Phys.)* 61, 8793.
- Katsura, T., Ito, E., 1989. The system Mg_2SiO_4 – Fe_2SiO_4 at high pressures and temperatures: precise determination of stabilities of olivine, modified spinel, and spinel. *J. Geophys. Res.: Solid Earth* (1978–2012) 94 (B11), 15663–15670.
- Katsura, T., Yamada, H., Nishikawa, O., Song, M., Kubo, A., Shinmei, T., Yokoshi, S., Aizawa, Y., Yoshino, T., Walter, M., 2004. Olivine/wadsleyite transition in the system (Mg, Fe) $_2\text{SiO}_4$. *J. Geophys. Res.: Solid Earth* 109 (B2).
- Katsura, T., Yamada, H., Shinmei, T., Kubo, A., Ono, S., Kanzaki, M., Yoneda, A., Walter, M.J., Ito, E., Urakawa, S., Funakoshi, K., Utsumi, W., 2003. Post-spinel transition in Mg_2SiO_4 determined by high P-T in situ X-ray diffractometry. *Phys. Earth Planet. Inter.* 136 (1–2), 11–24.
- Kohn, W., Sham, J.J., 1965. Self-consistent equations including exchange and correlation effects. *Phys. Rev.* 140, 1133.
- Kresse, G., Furthmüller, J., 1996. Efficient iterative schemes for ab initio total-energy calculations using a plane-wave basis set. *Phys. Rev. B* 54, 11169–11186.
- Kresse, G., Joubert, D., 1999. From ultrasoft pseudopotentials to the projector augmented-wave method. *Phys. Rev. B* 59, 1758–1775.
- Kroll, H., Kirfel, A., Heinemann, R., Barbier, B., 2012. Volume thermal expansion and related thermophysical parameters in the Mg, Fe olivine solid-solution series. *Eur. J. Miner.* 24 (6), 935–956.
- Kroumova, E., Aroyo, M.I., Perez-Mato, J.M., Kirov, A., Capillas, C., Ivantchev, S., Wondratschek, H., 2003. Bilbao crystallographic server: useful databases and tools for phase transition studies. *Phase Transitions* 76 (1–2), 155–170.
- Kudoh, Y., Takeuchi, Y., 1985. The crystal-structure of forsterite Mg_2SiO_4 under pressure up to 149 kBar. *Z. Krist.* 171 (3–4), 291–302.
- Li, L., Wentzcovitch, R.M., Weidner, D.J., Silva, C.R.S.D., 2007. Vibrational and thermodynamic properties of forsterite at mantle conditions. *J. Geophys. Res.* 112 (B5), B05206.
- Litasov, K., Ohtani, E., Sano, A., Suzuki, A., Funakoshi, K., 2005. In situ X-ray diffraction study of post-spinel transformation in a peridotite mantle: implication for the 660-km discontinuity. *Earth Planet. Sci. Lett.* 238 (3–4), 311–328.
- Lu, R., Hofmeister, A.M., 1994. Infrared spectroscopy of CaGeO_3 perovskite to 24 GPa and thermodynamic implications. *Phys. Chem. Miner.* 21, 78.
- Lu, R., Hofmeister, A.M., Wang, Y., 1994. Thermodynamic properties of ferromagnesian silicate perovskites from vibrational spectroscopy. *J. Geophys. Res.: Solid Earth* 99, 11795.
- Matsui, T., Manghni, M.H., 1985. Thermal expansion of single-crystal forsterite to 1023 K by Fizeau interferometry. *Phys. Chem. Miner.* 12, 201.
- McMillan, P., Ross, N., 1988. The raman-spectra of several orthorhombic calcium-oxide perovskites. *Phys. Chem. Miner.* 16 (1), 21–28.
- McMillan, P.F., Akaogi, M., 1987. Raman spectra of β – Mg_2SiO_4 (modified spinel) and γ – Mg_2SiO_4 (spinel). *Am. Miner.* 72 (3–4), 361–364.
- Monkhorst, H.J., Pack, J.D., 1976. Special points for Brillouin-zone integrations. *Phys. Rev. B* 13, 5188–5192.
- Morishima, H., Kato, T., Suto, M., Ohtani, E., Urakawa, S., Utsumi, W., Shimomura, O., Kikegawa, T., 1994. The phase boundary between α and β – Mg_2SiO_4 determined by in situ X-ray observation. *Science* 265 (5176), 1202–1203.
- Murnaghan, F.D., 1944. The compressibility of media under extreme pressures. *Proc. Natl. Acad. Sci. USA* 30 (9), 244–247.
- Noel, Y., Catti, M., D'arco, P., Dovesi, R., 2006. The vibrational frequencies of forsterite Mg_2SiO_4 : an all-electron ab initio study with the CRYSTAL code. *Phys. Chem. Miner.* 33 (6), 383–393.
- Oganov, A.R., Gillan, M., Price, G.D., 2005. Structural stability of silica at high pressures and temperatures. *Phys. Rev. B* 71 (6), 064104.
- Ono, S., Katsura, T., Ito, E., Kanzaki, M., Yoneda, A., Walter, M.J., Urakawa, S., Utsumi, W., Funakoshi, K.-I., 2001. In situ observation of ilmenite-perovskite phase transition in MgSiO_3 using synchrotron radiation. *Geophys. Res. Lett.* 28, 835.
- Ottone, G., Civalieri, B., Ganguly, J., Zuccolini, M.V., Noel, Y., 2009. Thermophysical properties of the α – β polymorphs of Mg_2SiO_4 : a computational study. *Phys. Chem. Miner.* 36 (2), 87–106.
- Parlinski, K., Kawazoe, Y., 2000. Ab initio study of phonons and structural stabilities of the perovskite-type. *Eur. Phys. J. B* 16, 49.
- Perdew, J.P., Burke, K., Ernzerhof, M., 1996. Generalized gradient approximation made simple. *Phys. Rev. Lett.* 77, 3865–3868.
- Piekarz, P., Jochym, P.T., Parlinski, K., Łazewski, J., 2002. High-pressure and thermal properties of γ – Mg_2SiO_4 from first-principles calculations. *J. Chem. Phys.* 117 (7), 3340.
- Presnall, D.C., Weng, Y.H., Milholland, C.S., Walter, M.J., 1998. Liquidus phase relations in the system MgO – MgSiO_3 at pressures up to 25 GPa – constraints on crystallisation of a molten Hadean mantle. *Phys. Earth Planet. Inter.* 107, 83–95.
- Reynard, B., Rubie, D., 1996. High-pressure, high-temperature Raman spectroscopic study of ilmenite-type MgSiO_3 . *Am. Miner.* 81 (9–10), 1092–1096.
- Robie, R., Hemingway, B., Takei, H., 1982. Heat capacities and entropies of Mg_2SiO_4 , Mn_2SiO_4 and Co_2SiO_4 between 5 and 380 K. *Am. Miner.* 67, 470–482.
- Ross, N.L., Hazen, R.M., 1990. High-pressure crystal chemistry of MgSiO_3 perovskite. *Phys. Chem. Miner.* 17, 228.
- Setyawan, W., Curtarolo, S., 2010. High-throughput electronic band structure calculations: challenges and tools. *Comput. Mater. Sci.* 49 (2), 299–312.
- Shim, S.-H., Duffy, T.S., Shen, G., 2001. The post-spinel transformation in Mg_2SiO_4 and its relation to the 660-km seismic discontinuity. *Nature* 411, 571.
- Sinogeikin, S.V., Bass, J.D., 2002. Elasticity of majorite and a majorite-pyropite solid solution at high pressure: implications for the transition zone. *Geophys. Res. Lett.* 29 (2), 1017.
- Stephens, P., Devlin, F., Chabalowski, C., Frisch, M., 1994. Ab initio calculation of vibrational absorption and circular dichroism spectra using density functional force fields. *J. Chem. Phys.* 98, 11623–11627.
- Stixrude, L., Lithgow-Bertelloni, C., 2011. Thermodynamics of mantle minerals – II. Phase equilibria. *Geophys. J. Int.* 184 (3), 1180–1213.
- Suzuki, A., Ohtani, E., Morishima, H., Kubo, T., Kanbe, Y., Kondo, T., Okada, T., Terasaki, H., Kato, T., Kikegawa, T., 2000. In situ determination of the phase boundary between wadsleyite and ringwoodite in Mg_2SiO_4 . *Geophys. Res. Lett.* 27 (6), 803–806.
- Suzuki, I., 1975. Thermal expansion of periclase and olivine and their anharmonic properties. *J. Phys. Earth* 23, 145–159.
- Trots, D.M., Kurnosov, A., Ballaran, T.B., Frost, D.J., 2012. High-temperature structural behaviors of anhydrous wadsleyite and forsterite. *Am. Miner.* 97, 1582–1590.
- Wang, S.Y., Sharma, S., Cooney, T.F., 1993. Micro-Raman and infrared spectral study of forsterite under high pressure. *Am. Miner.* 78 (5–6), 469–476.

- Wang, Y., Perdew, J.P., 1991. Correlation hole of the spin-polarised electron-gas, with exact small-wave-vector and high-density scaling. *Phys. Rev. B* 44, 13298–13307.
- Watanabe, H., 1982. Thermochemical properties of synthetic high-pressure compounds relevant to the Earth's mantle. In: Akimoto, S., Manghnani, M.H. (Eds.), *High Pressure Research in Geophysics*.
- Wentzcovitch, R.M., Yu, Y.G., Wu, Z., 2010. Thermodynamic properties and phase relations in mantle minerals investigated by first principles quasiharmonic theory. *Rev. Miner. Geochem.* 71 (1), 59–98.
- Williams, Q., Jeanloz, R., McMillan, P.F., 1987. Vibrational spectrum of MgSiO_3 perovskite: Zero-pressure Raman and mid-infrared spectra to 27 GPa. *J. Geophys. Res.* 92, 8116.
- Wu, Z., Wentzcovitch, R.M., 2007. Vibrational and thermodynamic properties of wadsleyite: a density functional study. *J. Geophys. Res.* 112 (B12), B12202.
- Yamanaka, T., Fukuda, T., Mimaki, J., 2002. Bonding character of SiO_2 stishovite under high pressures up to 30 GPa. *Phys. Chem. Miner.* 29 (9), 633–641.
- Yamanaka, T., Komatsu, Y., Sugahara, M., Nagai, T., 2005. Structure change of MgSiO_3 , MgGeO_3 , and MgTiO_3 ilmenites under compression. *Am. Miner.* 90, 1301–1307.
- Ye, Y., Brown, D.A., Smyth, J.R., Panero, W.R., Jacobsen, S.D., Chang, Y.-Y., Townsend, J.P., Thomas, S.-M., Hauri, E.H., Dera, P., Frost, D.J., 2012. Compressibility and thermal expansion of hydrous ringwoodite with 2.5(3) wt% H_2O . *Am. Miner.* 97 (4), 573–582.
- Ye, Y., Gu, C., Shim, S.H., Meng, Y., Prakapenka, V., 2014. The postspinel boundary in pyrolytic compositions determined in the laser-heated diamond anvil cell. *Geophys. Res. Lett.* 41, 3833–3841.
- Yu, Y.G., Wentzcovitch, R.M., 2006. Density functional study of vibrational and thermodynamic properties of ringwoodite. *J. Geophys. Res. Solid Earth* 111 (B12), B12202.
- Yu, Y.G., Wentzcovitch, R.M., Tsuchiya, T., Umemoto, K., Weidner, D.J., 2007. First principles investigation of the postspinel transition in Mg_2SiO_4 . *Geophys. Res. Lett.* 34 (10), L10306.
- Yu, Y.G., Wu, Z., Wentzcovitch, R.M., 2008. $\alpha - \beta - \gamma$ transformations in Mg_2SiO_4 in Earth's transition zone. *Earth Planet Sci. Lett.* 273 (1-2), 115–122.
- Yu, Y.G., Wentzcovitch, R.M., Vinograd, V.L., Angel, R.J., 2011. Thermodynamic properties of MgSiO_3 majorite and phase transitions near 660 km depth in MgSiO_3 and Mg_2SiO_4 : a first principles study. *J. Geophys. Res. Solid Earth* 116, B02208.
- Yusa, H., Akaogi, M., Ito, E., 1993. Calorimetric study of MgSiO_3 garnet and pyroxene – heat capacities, transition enthalpies, and equilibrium phase relations in MgSiO_3 at high pressures and temperatures. *J. Geophys. Res.* 98, 6453.